Thesis for the Degree of Doctor Philosophy

Digital Light Processing Printing of Silk Fibroin-based Structures for Microneedles and Light Harvesting Films

디지털 광원 처리 프린팅을 이용한 실크 피브로인 기반 마이크로니들 및 수광 필름 제조 연구

February 2023

Seoul National University
Department of Biosystems & Biomaterials
Science and Engineering

Shin, Donghyeok

Digital Light Processing Printing of Silk Fibroin-based Structures for Microneedles and Light Harvesting Films

Advised by Prof. Hyun, Jinho

Submitting a Ph.D. Dissertation of Agriculture
December 2022

Seoul National University
Department of Biosystems & Biomaterials
Science and Engineering

Shin, Donghyeok

Confirming the Ph.D. Dissertation written by
Shin, Donghyeok

February 2023

Chair Ki, Chang Seok (Seal)
Vice Chair Hyun, Jinho (Seal)
Examiner Kim, Tae-il (Seal)
Examiner Kwak, Seon Yeong (Seal)
Examiner Yun, Kyusik (Seal)

Abstract

Silk fibroin (SF) is a natural protein material that is currently used in various fields due to its high biocompatibility. Since the photocrosslinking reaction mechanism of SF molecules using riboflavin was recently reported, research on 3D printing of SF using digital light processing (DLP) technology has been actively conducted. As a photoinitiator, riboflavin absorbs light in the 350-450 nm region to form radicals, and at this time, SF forms dityrosine bonds through photo-oxidation to form a hydrogel network. The use of riboflavin in the photocrosslinking reaction of SF is quite challenging and few previously studied cases. However, it is worth researching as it is possible to fabricate a 3D printed structure that is highly biocompatible and maintains its shape only with SF and riboflavin. In addition to exploiting the photocrosslinking reaction of SF, the introduction of an anti-aliasing strategy in DLP printing can improve the resolution of SF patterns by reducing stair effects. Since resolution is a hardware limitation of equipment used in DLP printing, image processing processes such as grayscale processing and image adjustment in pixel units are required to improve resolution. In this study, the hardware limitations of DLP projector resolution were overcome through customized grayscale processing software. The improved resolution of the SF 3D printed structure is evaluated through the smaller and sharper microneedle structure. In this study, a SF microneedle was fabricated and its performance was evaluated through a penetration test on pig skin. In addition, the process of creating a 3D model for DLP printing can be omitted through image adjustment in pixel units. Since the DLP pattern image is a two-dimensional bitmap, the image can be scaled pixel by pixel to print a structure of the desired shape, which is verified by creating a relatively large size structure. In this study, an optical film structure for light harvesting was fabricated and light diffraction characteristics were investigated. It was confirmed that a minimum of 1.62% and a maximum of 6.74% more voltage was produced in the photovoltaic cell using the fabricated SF optical film structure. This research will serve as an opportunity to broaden the application field of protein-based ink by presenting the experimental results for DLP printing of SF.

Keyword: Silk Fibroin, 3D Printing, Digital Light Processing, Anti-aliasing, Microneedles, Optical Film.

Student Number: 2016-21475

Table of Contents

List of Figures

I. Introduction

Silk fibroin (SF) is regenerated protein present in the cocoon of silkworm *Bombyx mori* [1]. Currently, SF is a widely known material in several fields, including tissue engineering [2], and regenerative medicine [3], electronics [4], and optics [5] due to its biocompatibility and excellent mechanical performance [6]. Also, SF is an FDA-approved biomaterial for surgical scaffold material [7]. Amino acids in SF are mostly glycine (45.9%) and alanine (30.3%), which have low chemical reactivity. However, some amino acids, such as tyrosine (5.3%), can be chemically crosslinked [1].

SF is a biopolymer with good biocompatibility and excellent mechanical strength [8]. Also, it is transparent and applicable as an optical material for lenses and diffraction gratings [9]. SF can form hydrogels by various crosslinking mechanisms, and its hydrogels can be formed by photocrosslinking reactions. SF can be photocrosslinked by various methods such as photo-oxidation and free radical methacrylate polymerization [1]. These characteristics of SF motivated studies to determine whether it can be used for 3D printing ink materials.

As one of the representative methods for utilizing photo-oxidation, Ru(II)/persulfate can be used to cause photocrosslinking of SF [10]. Ru(II)/persulfate helps tyrosine of SF, gelatin, and fibrin form dityrosine bonds. However, biocompatibility of ruthenium is still being investigated [1]. As Ru(II)/persulfate does not contribute in the network of SF hydrogels, it must be removed after reaction to avoid potential biohazards.

When SF is chemically modified through methacryloyl modification, the hydrogel can be produced using free radical polymerization. Methods for imparting methacryloyl functional groups to SF using methacrylic anhydride or glycidyl methacrylate are already known. When methacrylic anhydride is used, the crystallization of SF is induced [11]. SF modified with methacryloyl modification can be characterized by a rapid photocrosslinking reaction.

Interestingly, a new strategy using riboflavin as a photoinitiator has been reported [8]. Riboflavin, also called vitamin B2, is a nutrient found in natural tissues. Riboflavin plays a significant role as a photoinitiator in forming SF hydrogels because it can be used alone without any other additives [1]. Besides, it is less biohazard compared to Ru(II)/persulfate. However, the reaction time is a little longer from several minutes or more when it is used alone as a photoinitiator. Fortunately, the slow crosslinking kinetics of riboflavin can be improved by the addition of sodium persulfate.

3D printing is one type of additive manufacturing technology for designing complex structures or shapes based on 3D model data [12]. First 3D printing is considered to be stereolithography technique invented by Charles Hull [13-15]. Since then, new 3D printing technologies such as powder bed fusion [16], fused deposition modeling [17], and inkjet 3D printing [18] have been developed. Even in recent years, new cases using various methods, materials, and equipment continue to be reported in the field of 3D printing research. The advantage of 3D printing technology is multi-item, small-volume production which is also expressed in mass customization [12]. Because 3D printing is mass customization method, prices can be kept low, and individual products can be produced because each product is different. Also, 3D printing does not require molds or tooling to build products so the manufacturing costs can be reduced.

As 3D printing technology develops, material savings and high precision are highlighted. Materials currently used in 3D printing include metals, polymers, ceramics and concrete. The versatility of materials demonstrates that 3D printing is advancing in many fields. However, there is also an opinion that diversity of materials should be further expanded. 3D printing can also produce structures of various sizes from microscale to macroscale. However, precision also depends on 3D printing method and scale size. For microscale 3D printing, there are also resolution and surface finish issues [19].

Stereolithography (SLA) printing is an additive manufacturing strategy developed in 1986 [13-15]. In principle, it continuously laminates layers with photocrosslinking reaction of polymer monomer solution using light energy. A monomer is activated by light to become radical and then polymer chain. At this time, the remaining unreacted monomers are removed, and the result of stacking becomes a 3D-printed structure. SLA printing enables the production of high-quality structures with resolutions down to 10 micrometers [20]. At this time, the energy amount of light source and photocrosslinking time are main variables when fabricating layers [15]. However, it is expensive to operate and the printing speed is slow compared to other 3D printing methods. Also, since printable materials are limited, it is necessary to discover various other material candidates.

The principle of DLP printing is considered to be an extension of the principle of SLA printing [21]. The most important difference is that DLP printing can project an image of pattern over large area to form one layer at a time. Since a pattern image is a contiguous set of pixels, a layer is formed from contiguous set of voxels. SLA printing uses laser, so it takes time for laser to move to form one layer, but because DLP printing forms one layer at a time, the printing speed is faster than SLA. The digital micromirror device in DLP projectors makes it possible [22]. The digital micromirror device is a component that enables irradiation of pattern image adjusted in pixel units on monomer solution.

Since a new photocrosslinking strategy using SF and riboflavin was reported [8], studies with SF as DLP printing ink have been continuously reported [23, 24]. SF has already been verified as an excellent material in many fields. Riboflavin continues to be studied as photoinitiator in an effort to reduce reliance on petroleum-based materials [25]. In this respect, SF and riboflavin are promising as SLA/DLP printing materials and are chosen for the 3D printing ink material in this study.

In DLP printing, pattern images are reprojected onto a monomer solution to form a layer by causing a photocrosslinking reaction in the area where the light energy reaches. The digital micromirror device in a DLP projector adjusts the brightness of projected image by changing the on/off state [26]. Therefore, the brightness of the projected image per time can be adjusted, by modifying the pixel value of pattern image itself.

This method is called grayscale lithography or grayscale digital light processing [26-28]. This method adjusts the light exposure dosage by adjusting the brightness of each pixel. In the Microsoft Windows environment, 256-level grayscale images can be expressed without special preparation. Pattern image can be expressed by assigning each pixel light intensity from the darkest (black, 0.0) to the brightest (white, 1.0) of DLP projector. By applying grayscale lithography, it is possible to print a structure whose size is smaller than 1 pixel or to print structures with non-uniform photocrosslinking density within the same layer [29]. Using Pillow library provided in Python programming language, researcher can easily create pattern images whose brightness is adjusted in pixel units, and easily apply image processing techniques for grayscale lithography. Therefore, in this study, a customized program is created using Python and Pillow to create SF-based microneedles and SF-based optical films, and pattern images are created.

Microneedles are one of the transdermal drug delivery systems that are hundreds of micrometers long [30]. The purpose of using microneedles is to penetrate skin without pain and increase skin permeability for drugs. Increased skin permeability allows small molecules to pass through it [30-33]. Microneedles are usually manufactured through complex micromachining processes. Examples include surface micromachining [34, 35] and etching [36-38]. These subtractive manufacturing methods are not suitable for controlling topological diversity. This is because the subtractive manufacturing method itself has problems related to processing, complexity and high cost [39-42]. Compared to subtractive manufacturing methods, additive manufacturing methods allow geometrical control of 3D structures at microscale through layer-by-layer systems [43-45]. Also, drawing lithography using some polymers has been reported [46, 47]. This method is a method of fabricating a microneedle by using the glass transition and viscous properties of the polymer while stretching the polymer. This method is one of the good alternatives to subtractive manufacturing, but it is also limited in the shapes that can be made and the materials that can be used.

Among additive manufacturing methods, 3D printing is the strategy developed for structuring various materials, including powders, filaments, suspensions, and crosslinkable polymer solutions [39-44]. Various types of materials have been used to fabricate microneedles, such as silicon [48], metal [49], and polymer resin, etc. [41, 50]. Among various application fields of microneedles, the biocompatibility and safety of materials must be considered for medical microneedles. If a microneedle is made of protein-based biomaterial, it is expected that immunological risk caused by microneedle damage during skin penetration can be significantly reduced. Recently, microneedles using SF protein extracted from the cocoons of *Bombyx mori* have been reported [51-54]. Microneedles can be fabricated by applying multi-step molding and curing process to SF protein. Because general microneedles are manufactured through molding process, it is difficult to apply protein-based materials to these processes. High crystallinity of protein-based materials may lead to decomposition rather than melting at high temperatures.

In general, the strategy for fabricating structures using 3D printing is not suitable for fabricating microneedles [39, 55]. Limitations of this strategy also appear when microneedles are produced using DLP printing. Most of all, the resolution of DLP projector in DLP printing is considered a main hardware limitation. Hardware limitation of resolution can be overcome by software improvement through grayscale processing. In other words, fabricating small and sharp structures such as microneedles through DLP printing is considered important attempt to overcome limitations of DLP printing and 3D printing.

Currently, energy production relies on fossil fuels such as coal, crude oil and natural gas, which are limited mined resources. Due to the global warming crisis, increase in global energy demand and resulting environmental problems, the interests in developing alternative energy resources are increasing [56]. As an alternative energy collector, photovoltaic (PV) devices have potential for converting light into electrical energy [56, 57]. Among the various solar cell types, multi-junction solar cells receive light over a wide area and produce electrical energy, so they have excellent energy conversion efficiency. Higher energy conversion efficiency can be achieved even if the light that does not directly reach PV panels can be harvested [56].

In addition, the importance of eco-friendly materials is currently being emphasized in optoelectronic industry [57]. SF is not a simple natural material, but is being studied as an eco-friendly future material including manufacturing process [58]. It has been recognized that SF is environmentally sustainable and it can be a candidate material for new solar cell application materials. In addition, pattern images do not have to be 3D model, but can be expressed in intended shape in the wide area through pixel unit control. Transparency of SF and the patterned film structure induces the diffraction of light, which will increase the efficiency of photovoltaic devices producing more electrical energy.

In this study, the feasibility of DLP printing with the SF-riboflavin ink is shown by the fabrication of microneedles and microstructured optical films (Figure 1). It is challenging because it creates sharp microstructures without an expensive template and the control of light direction by the simple microstructure at the surface. It will provide a sort of ideas for future research with eco-friendly biomaterials for the biomedical and optical applications.

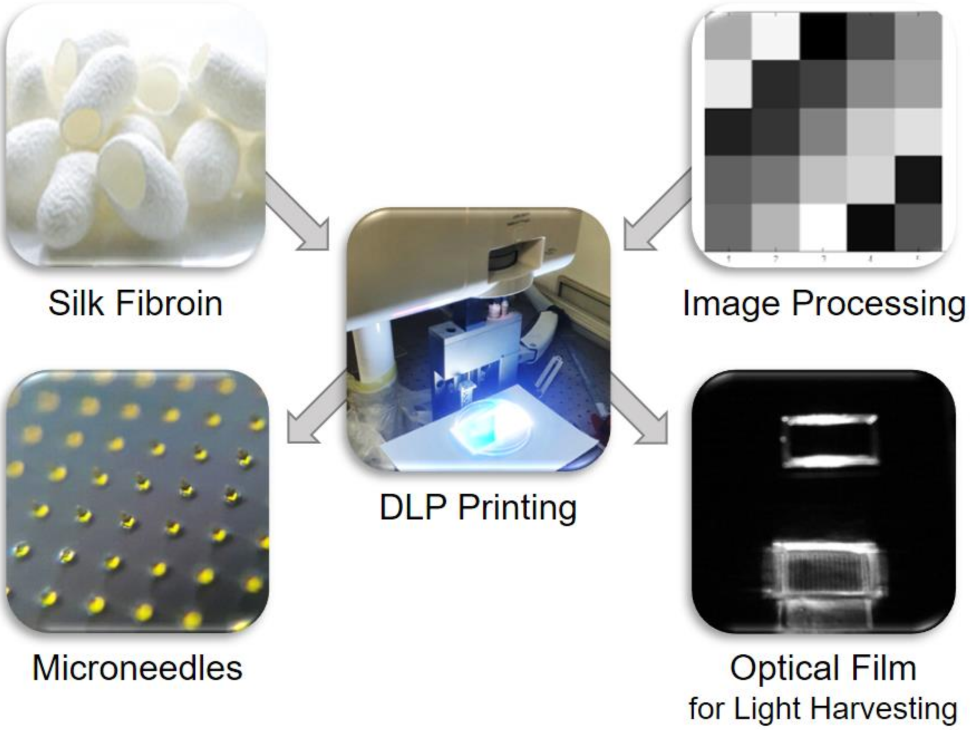

Figure 1. Flow chart of the entire study. DLP 3D printing is performed using refined silk fibroin ink materials and image files processed by image processing. The improved printing resolution is verified through a fabrication of the SF microneedle, and the ability to adjust the image in pixel units in a wide area is verified through a fabrication of the SF optical film.

II. Materials and Methods

2.1. Preparation of Silk Fibroin

The preparation method of SF aqueous solution was established by modifying experiments reported in the literature [59]. *Bombyx mori* cocoon was degummed to remove silk sericin from cocoon and obtain SF fibers. For this, 40 g of cocoon, 3 g of sodium oleate (Sigma-Aldrich, St. Louis, MO, USA), and 2 g of sodium carbonate (Sigma-Aldrich, St. Louis, MO, USA) were added to 1 L of water and heated at 85 °C for 1 h to obtain SF fibers. SF fibers were dried in an oven at 80 °C for more than 48 h to remove moisture. 140 ml solution of 28 g of dried SF fibers and 9.3 M lithium bromide (Kanto Chemical, Tokyo, Japan) aqueous solution was boiled at 80 °C for 1 h to dissolve SF. Then, SF/lithium bromide solution was dialyzed in deionized water for more than 48 h using 12-14 kDa cutoff dialysis membrane to obtain a 6-7 wt% SF aqueous solution. Finally, impurities remaining in the SF aqueous solution were removed by filtering using Miracloth (pore size of 22-25 μm, Merck Milipore, Burlington, MA, USA).

2.1.1. Absorbance of Silk Fibroin Solutions and Films

The absorbance of SF solutions were measured at regular time intervals using UV/Vis equipment (UV/Vis Spectrophotometer, Optizen POP, KLAB, Republic of Korea), every day while maintaining the samples at 5 °C in a refrigerator. The absorbance of SF films were measured using UV/Vis equipment (UV/Vis Spectrophotometer, Optizen POP, KLAB, Republic of Korea).

2.1.2. Chemical Structure of Silk Fibroin Solutions and Films

Fourier transform infrared (FT-IR) spectroscopy (Nicolet iS5, Thermo Scientific, Waltham, MA, USA) was used to determine the formation of beta sheets in the SF aqueous solutions and films. The scan number was 32 with a resolution of 4 cm^{-1} in the wavenumber range of 1700 to 1600 cm^{-1}.

2.2. Preparation of DLP Printing System

SF structures were fabricated with a customized top-down DLP printing system. The cover glass was fixed to the platform, and images were projected using a commercial projector (DH976WT, Vivitek, Fremont, CA, USA). Also, polyethylene terephthalate (PET), polyvinyl chloride (PVC), aluminum foil and cellophane tape were used. The z-Position of printing platform was adjusted through LabVIEW program (National Instruments, USA), and custom AutoHotkey program (AutoHotkey Foundation LLC, USA) was used for controlling LabVIEW program. The digital images for printing were created using custom program written in Python 3.5 (Python Software Foundation, USA). Program to generate grayscale images for microneedle fabrication and program to generate pattern images for fabrication of optical films were written respectively. All digital images were continuously projected using slideshow function of ArtSage 2.0 (Rick Xavier (Xworks), Canada). The amount of light energy generated by DLP projector was measured using an accumulated UV meter. (UIT-250, Ushio, Tokyo, Japan)

2.3. Fabrication of Microneedles

2.3.1. Fabrication of Silk Fibroin Microneedles

To explore the concentration conditions of SF-based DLP printing ink, the inks at 2, 4, and 6 wt% aqueous SF solution and 0.5 mM riboflavin were prepared at room temperature. SF microneedles were fabricated with a custom top-down DLP printing system. SF microneedles were printed under condition that height of each layer was 10 μm. Photocrosslinking time per layer was set to 150 s and total number of layers was 100. Riboflavin remaining after SF hydrogel printing was removed by washing with deionized water. After washing, SF hydrogels were dried in the oven at 80 °C for 15 min. Then, the fabrication of SF microneedles was completed. All SF microneedles were stored in dehumidified environment.

2.3.2. Fluorescence Measurement of Silk Fibroin Hydrogels

Dityrosine bindings in SF hydrogel were measured using a microplate reader at 37°C (Synergy H1 Hybrid Multi-Mode Microplate Reader, BioTek, Winooski, VT, USA). Fluorescence was observed in the wavelength range of 380-480 nm under excitation at 310 nm.

2.3.3. Morphological Properties of Silk Fibroin Microneedles

Dried SF microneedles were examined using an optical microscope (Olympus, CKX-41, Tokyo, Japan). The surface of SF microneedles was observed by field emission scanning electron microscopy (FESEM, SUPRA 55VP, Carl Zeiss, Oberkochen, Germany). SF microneedles were coated with a thin platinum layer and then visualized by secondary electron detector at 10 kV.

2.3.4. Mechanical Properties of Silk Fibroin Microneedle

Compressive strength test of SF microneedle was performed using universal testing machine (Lloyd, Chichester, UK). Testing conditions were set at 10 N load cell, 100 mN preload stress, 1 mm/h preload speed, and 1 mm/min compression speed. For the compressive strength test, 3D printed SF microneedles with 150 μm base width and 500 μm needle height were used.

2.3.5. Penetration Test of Silk Fibroin Microneedles on Porcine Skin

SF microneedles for penetration test were prepared with single layer height of 10 μm and a total of 100 layers. SF films without needles to be used as control samples were prepared in single layer height of 100 μm and total of 5 layers. The photocrosslinking time for each layer was 150 s. Prepared microneedles and films were dried in an oven at 80 °C for 15 min to completely remove moisture. SF microneedles and SF films were coated with 0.01 wt% rhodamine B solution (Sigma-Aldrich, St. Louis, MO, USA) for 10 min. Before the penetration test, the surface of pig skin was coated with FITC (Sigma-Aldrich, St. Louis, MO, USA) for 10 min and then washed with water. Microneedles and films were placed on the surface of pig skin, and rhodamine B was delivered into skin by pressing at 300 mN for 10 min. After the penetration test, pig skins were embedded in optimal cutting temperature compound (O.C.T. Compound, Sakura Finetek USA, Torrance, CA, USA) and frozen at −70 °C for 40 min. Then, specimens having a thickness of 30 μm were prepared using cryostat-microtome (Leica CM1850, Wetzlar, Germany) at −25 °C. Penetrated surface and sections were imaged with optical microscope (Celena S, Logos Biosystems, Anyang, Republic of Korea) and digital camera (SM-N976 N, Samsung Electronics, Suwon, Republic of Korea) under UV illumination.

2.4. Fabrication of Optical Film for Light Harvesting

2.4.1. Fabrication of Silk Fibroin Optical Film for Light Harvesting

The SF-based DLP printing ink was prepared with 2, 4, and 6 wt% aqueous solutions. 0.5 mM riboflavin was used as a photoinitiator. SF aqueous solution and riboflavin were mixed at room temperature. SF optical films were fabricated with a custom top-down DLP printing system. Patterned structures on SF optical film were printed under conditions of monolayer heights of 200, 300, and 400 μm. Photocrosslinking time per layer was set to 15 min. Riboflavin remaining after SF hydrogel printing was removed by washing with deionized water. The washed SF hydrogel was dried at 80 °C for 15 min to form SF optical films. All SF optical films were stored in dehumidified environment.

2.4.2. Refractive Index of Silk Fibroin Optical Film

To measure the refractive index of SF optical films, 1 cm x 2 cm rectangular film was prepared and used. Refractive indices of all samples were measured using abbe refractometer. For comparison according to concentration of SF aqueous solution, film samples were prepared using 2, 4, and 6 wt% SF aqueous solutions containing 0.5 mM riboflavin. For comparison, film samples were prepared by setting photocrosslinking time to 5, 10, 15, and 20 min.

2.4.3. Various Pattern Formation on Silk Fibroin Optical Film

To confirm the feasibility of producing SF optical films, structures were fabricated using pattern images of various shapes. All pattern images were created using Microsoft Windows 10 Paint (Microsoft, Redmond, WA, USA). Basic shape (□, ○, ☆, and △), mosaic (1, 2, 3, 4, and 5 pixel), and stripe patterns were used as type of pattern image.

2.4.4. Light Diffraction Properties of Silk Fibroin Optical Film

The diffraction direction of light was confirmed according to the pattern shape on SF optical film. Total 8 different pattern shapes were created on the SF optical films, and the diffraction direction of light was observed with a red laser pointer (650 nm). Two lasers (red (650 nm) and green (532 nm)) were used to investigate the distance of the interference pattern according to the wavelength of light. Laser light was passed through a SF film with a single dot pattern, and the spacing of the interference pattern on the 1 mm squared graph paper was measured. The distance between the laser light source and the graph paper was set to 2 m.

2.4.5. Pattern Images for Fabrication of Patterned Silk Fibroin Films

Various pattern images were produced to measure the diffraction effect of light according to the pattern of SF optical film. To measure the effect according to pattern area, samples with 100%, 50%, and 25% of pattern area were prepared based on one closed line with the width of 5 pixels for a square shape. To measure the effect of the number of lines in pattern, samples with 1, 2, and 3 closed lines with a width of 5 pixels for a square shape were prepared. To measure the effect of different pattern widths, samples with three closed lines with widths of 3, 5, and 7 pixels for square shape were prepared. To measure the effect of the shape of pattern, samples with a width of 5 pixels and one closed line in shape of sin curve and zigzag line were prepared. Pattern images to measure the effect according to area, line, and width of pattern were created using Microsoft Windows 10 Paint (Microsoft, Redmond, WA, USA). Pattern images to measure the effect according to shape of pattern were produced using customized Python 3.5 (Python Software Foundation, USA) program.

2.4.6. Gray Value Analysis of Silk Fibroin Optical Film

In order to measure the effect of light diffraction according to pattern of SF optical film, pictures were taken using CCD sensor of digital single lens reflex (DSLR) camera (Nikon D70, Nikon, Japan). The distance between SF optical film and CCD sensor was set at 5 cm. Ambient illumination was controlled at 240 lux (Figure 2A). The sum of the gray values with 3 mm long straight line in the vertical direction from the boundary of the film pattern was determined using ImageJ (National Institutes of Health, USA) and the increase of the gray values was compared (Figure 2B).

2.4.7. Photovoltaic Panel Voltage Analysis of Silk Fibroin Optical Film

In order to measure the effect of diffracting light according to pattern of SF optical film, photovoltaic panel (Daduino, Siheung, Gyeonggi-do, Republic of Korea) was irradiated with light by DLP projector (DS23DAA, Vivitek, Fremont, CA, USA). A photovoltaic panel was masked with black insulating tape, leaving only area of 1.4 cm x 2.7 cm in size (3.8 cm^2). PV panel voltage values of each sample were recorded when the digital multimeter stopped its changing voltage. The distance between SF optical film and photovoltaic panel was set at 5 cm. Two types of light irradiation were used for photovoltaic panel voltage analysis. One uses an image that illuminates only the area of the SF optical film (Figure 3A), and the other uses an image that illuminates the entire area of the photovoltaic cell including the SF optical film (Figure 3B). The voltage generated by photovoltaic panel was measured using digital multimeter (PC7000, Sanwa Electric, Tokyo, Japan).

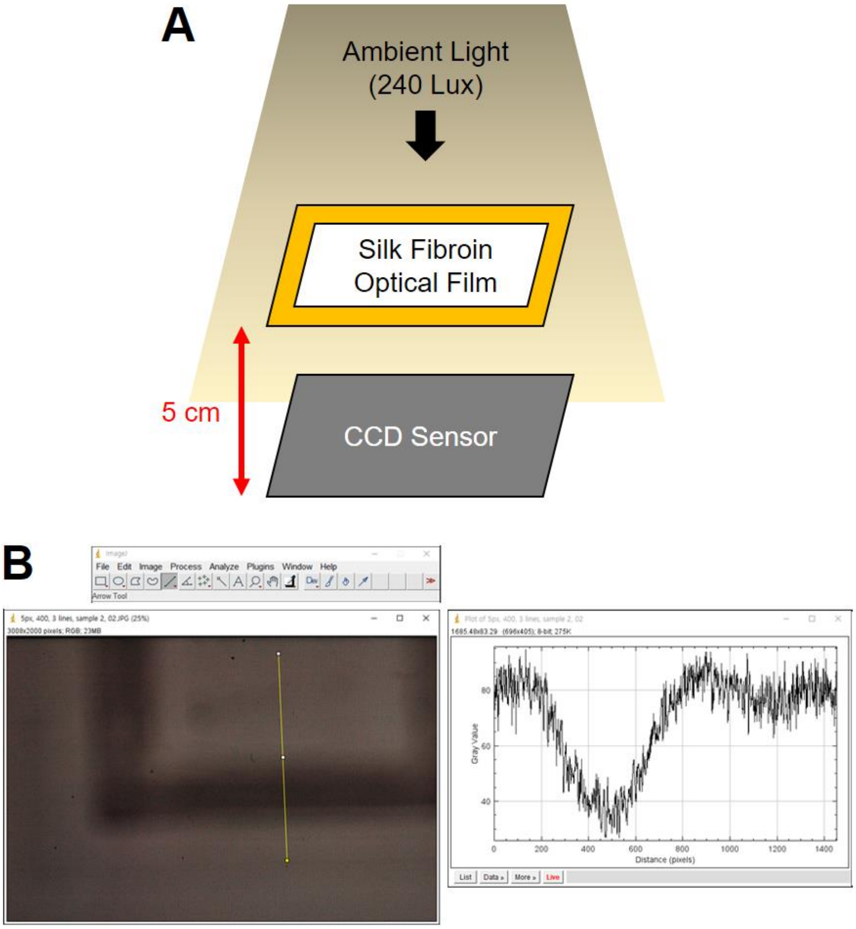

Figure 2. (A) Ambient light environment when shooting SF optical film with a CCD sensor. (B) A method of obtaining the changed gray value in the area where the gray value is increased. Generally, the curves show shoulder features that were not originally present.

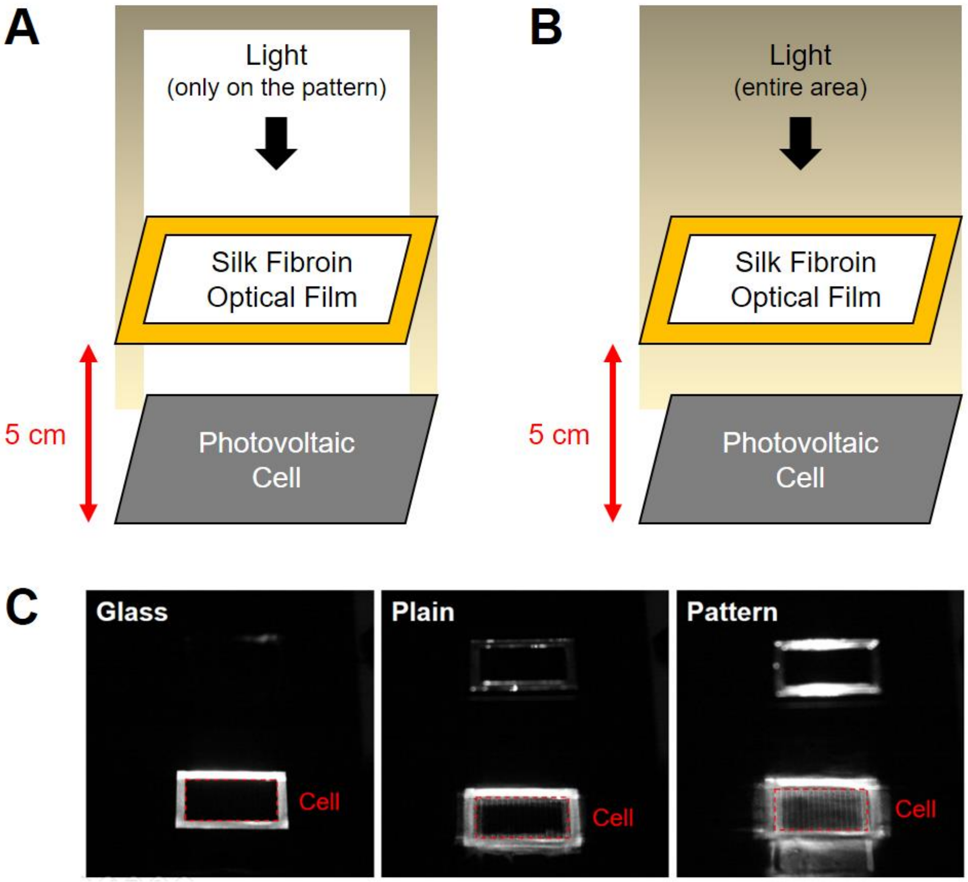

Figure 3. Scheme of photovoltaic panel voltage analysis. (A) When light is applied only on the pattern area of the film, (B) When light is applied to all areas. (C) When light is applied only on the patterned area of the film, the diffracted light is clearly observed.

III. Results and Discussion

3.1. Preparation of Silk Fibroin

Silk sericin was extracted from cocoon through degumming of *Bombyx mori* and only SF fibers were obtained. The drying process completely removes the moisture from SF fibers. SF fibers were dissolved in lithium bromide aqueous solution, and 6-7 wt% SF aqueous solution was obtained through dialysis. In order to continuously use SF aqueous solution as 3D printing ink in all subsequent experiments, the concentration of SF aqueous solution must be optimized. Since SF aqueous solutions sometimes form beta sheets and become solid hydrogels during storage, SF aqueous solutions of various concentrations were prepared to find an appropriate concentration for storage.

3.1.1. Properties of Silk Fibroin Solutions

Aqueous solutions of SF were diluted to 2, 4, and 6 wt%. Prepared SF aqueous solutions were refrigerated at 4 °C for 7 days immediately after preparation, and absorbance were measured every day. In order to achieve high resolution for DLP printing, light must be scattered as little as possible in the solution. Therefore, the most ideal result is that there is little change in absorbance of SF aqueous solution according to storage period. Figure 4 shows the absorbance measurement results. As a result of measurement, absorbance of 2, 4, and 6 wt% showed little change during the storage period of 7 days. In fact, as 3D printing ink, the SF aqueous solution is used up within 1 to 2 days, so maintaining absorbance of the SF aqueous solution stable for 7 days is proper for the printing.

In addition, FT-IR analysis confirmed whether the transition from SF aqueous solution to beta sheet had occurred. In the FT-IR analysis result, the presence or absence of transition to beta sheet can be determined by checking

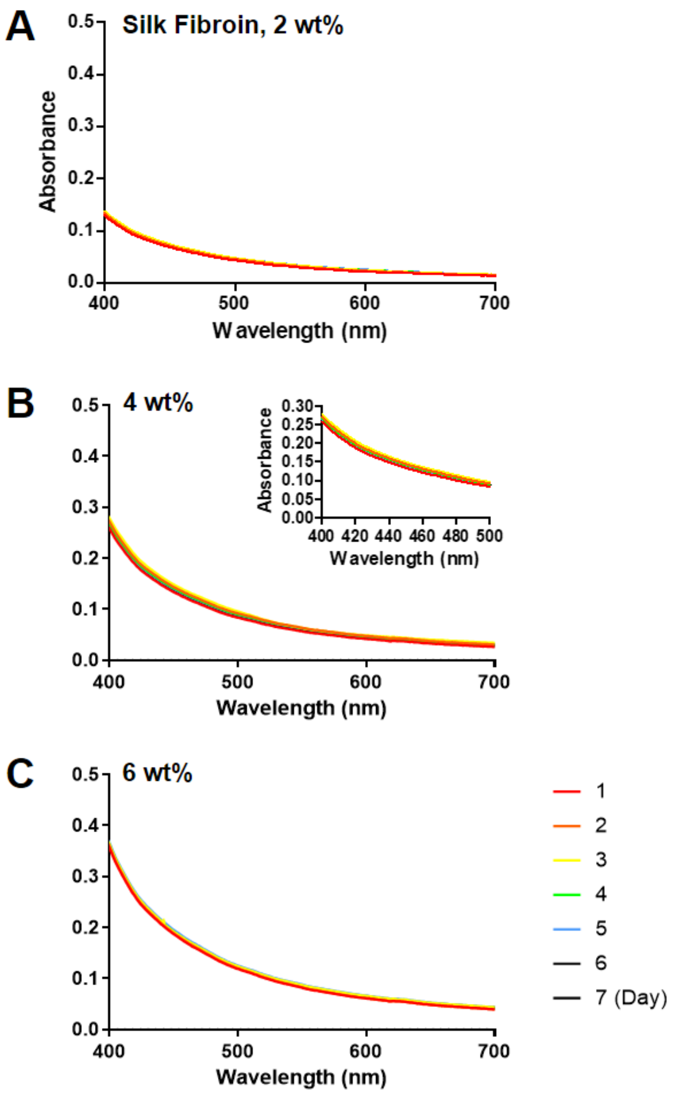

Figure 4. Changes in UV/Vis absorbance spectra in the range of 400-700 nm when aqueous solutions of SF of various concentrations were stored for 7 days. Absorbance spectra of (A) 2, (B) 4, and (C) 6 wt% SF solution. (Enlarged area: 400-500 nm)

amide I band region of SF (Figure 5). According to the results, the absorbance peak of samples stored for 7 days appeared at 1640 cm^{-1} and did not appear between 1620 and 1600 cm^{-1}. When SF forms beta sheet structure, an absorbance peak is observed in the range between 1620 and 1600 cm^{-1}. This means that there was no conversion to beta sheets in SF solution during the storage for 7 days. As described above, since the SF solution used in experiment was used up within 1 to 2 days, the beta sheet transition of SF solution was not critical during the 3D printing.

3.1.2. Properties of Silk Fibroin Films

All structures fabricated using SF solutions contain some riboflavin. Therefore, the effect of riboflavin on UV/Vis spectra was analyzed for various SF films by measuring the absorbance of each SF films. Changes in UV/Vis spectra were observed in the range of 400-500 nm. There was no significant difference in absorbance between the presence and absence of the beta-sheet. However, when riboflavin was included, an increase in absorbance occurred (Figure 6A). When silk films with the same thickness were prepared using SF solutions of various concentrations, the absorbance increased as the concentration of the SF solution increased. (Figure 6B) Since riboflavin is the same amount in each SF solution, the effect of riboflavin on UV/Vis spectra is different depending on the concentration of the SF solution. When the concentration of the SF solution was kept the same and only the amount of riboflavin was changed, the absorbance increased as the amount of riboflavin increased. (Figure 6C) This indicates that the absolute amount of riboflavin affected the UV/Vis spectra. Figure 6D is the result of 3D printing with the concentration of the SF solution where the amount of riboflavin the same, only the thickness of the film structure being different. The thicker the film, the higher the absorbance. The amount of riboflavin also had an effect.

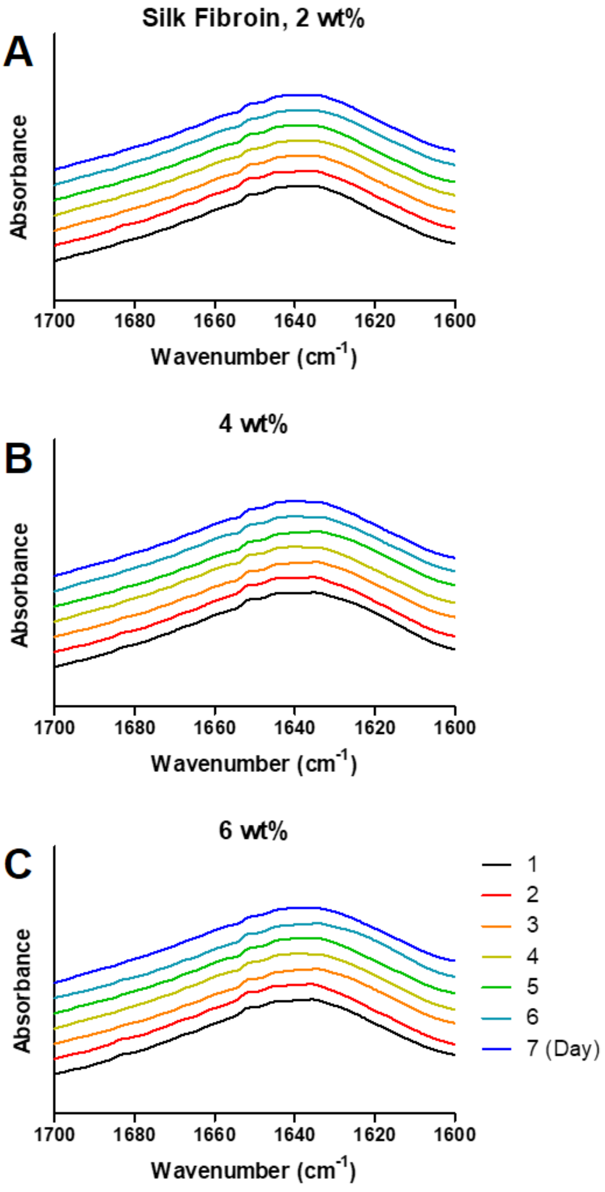

Figure 5. Changes in FT-IR absorbance when aqueous solutions of SF of various concentrations were stored for 7 days. Spectra of (A) 2 wt%, (B) 4 wt%, and (C) 6 wt% SF solution.

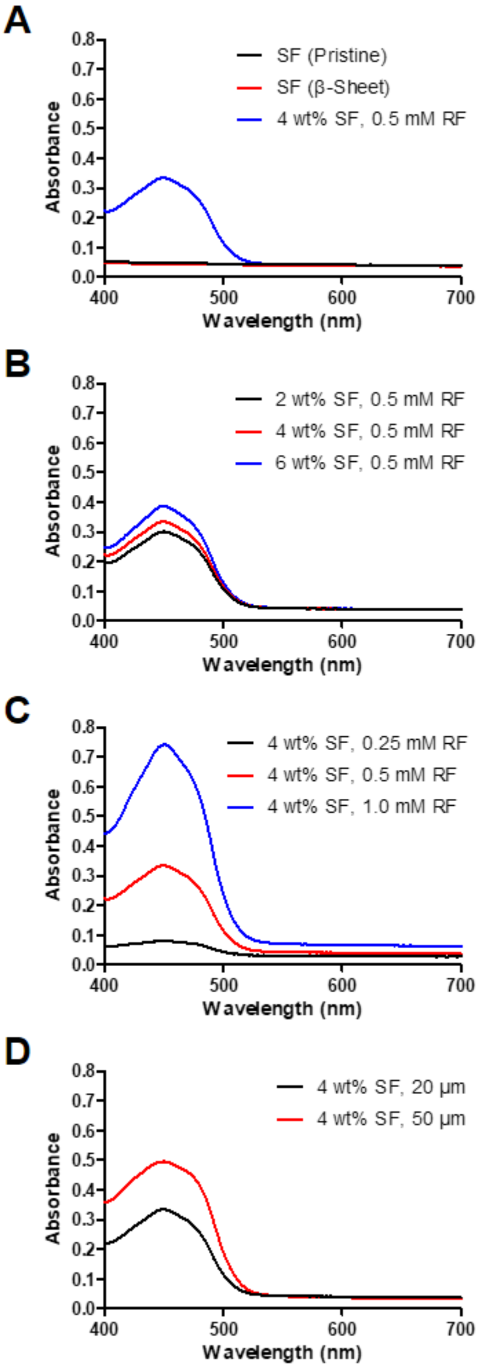

Figure 6. UV/Vis spectra of various SF films. (A) The results according to difference between normal pristine SF film, beta-sheet induced SF film, and printed SF optical film. The results according to differences in (B) SF solution concentrations, (C) riboflavin concentrations, and (D) SF film thickness.

Through FT-IR spectra analysis, no beta sheet was created on the SF structure before and after the 3D printing and drying/shrinkage processes. When a beta sheet is present in the SF film, a peak is observed at 1620 cm^{-1}. (Figure 7A) However, as a result of FT-IR analysis according to the concentration of the SF solution (Figure 7B), the concentration of riboflavin (Figure 7C), and the thickness of the SF film (Figure 7D), no beta sheet was made in any case.

The scattering effect of light helps to generate more electrical energy by allowing the light to linger around the photovoltaic cell. For example, previously reported studies using silk fibroin used beta sheets for light scattering effects. [57] However, the more beta sheets are present in SF solution, the more impurities are generated in printing, so it is not suitable for the DLP printing process. A solution containing impurities has a very negative effect on the shape of a 3D structure, so it is not suitable as a DLP printing ink. Therefore, in this study, the absence of beta sheets in the SF solution was avoided as much as possible.

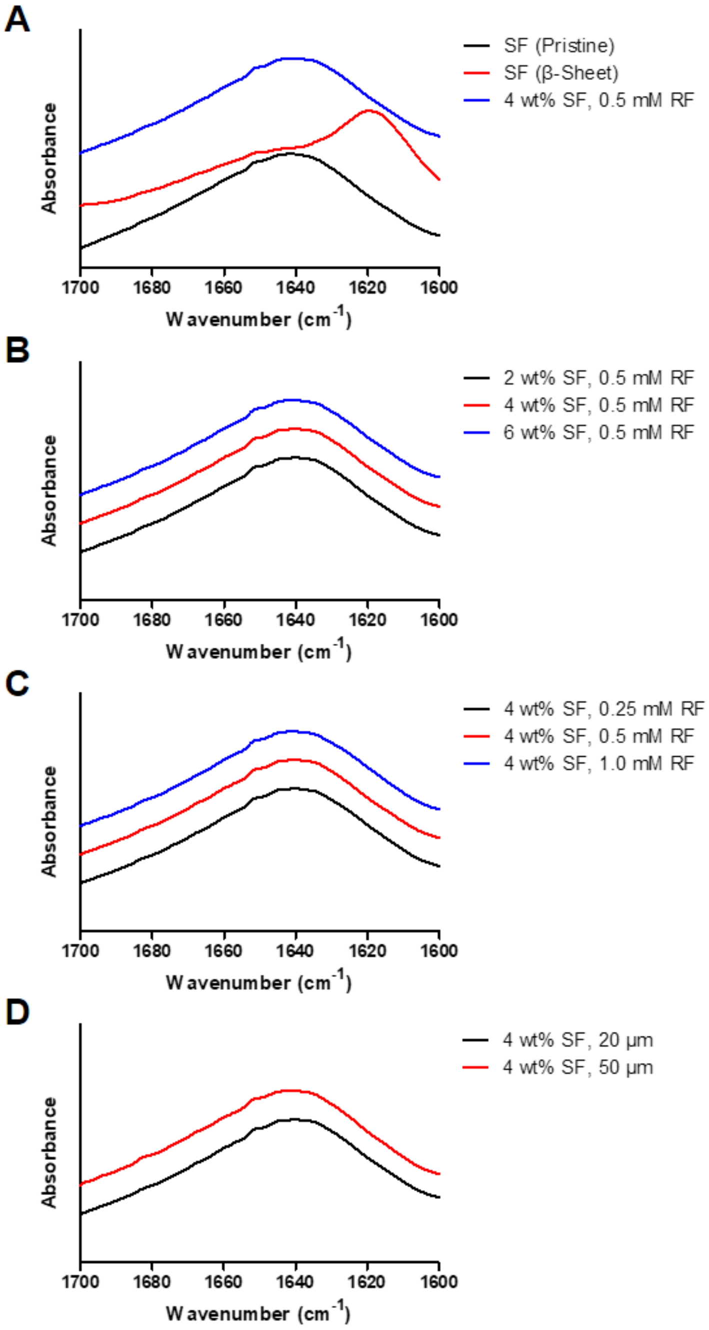

Figure 7. FT-IR spectra of various SF structures. (A) The results according to difference between normal pristine SF structures, beta-sheet induced SF structures, and printed SF optical structures. The results according to differences in (B) SF concentrations, (C) riboflavin concentrations, and (D) SF film thickness.

3.2. DLP Printing System

The operational scheme of DLP printer used in the experiment is as depicted in Figure 8. DLP printers work using two computers. Before starting with 3D printing, the operating system time of two computers was always synchronized to prevent time error between different devices.

Computer 1 was used to run the position controller to adjust z-position. The z-Position platform and glass platform were directly connected to position controller. Glass platform serves as a base to form a SF hydrogel. As a program to operate position controller, a customized program made with LabVIEW was used. Because this program was not an automatic program, it received z-position values manually and updated it. However, it was not appropriate to refactor LabVIEW-based customized program that had already been compiled, so Autohotkey-based customized program following flowchart of Figure 9 was created and used for the experiment. This program adjusted z-position of position controller by inputting the z-position coordinates to LabVIEW-based customized program according to certain time. Through this, Autohotkey-based program renewed the z-position of glass platform, eventually helping to enable top-down DLP printing. Autohotkey-based programs could be used by inputting total number of layers, height per layer, and photocrosslinking time per layer. Vat contained SF ink for 3D printing. After SF hydrogel was formed for each layer, the glass platform was placed in new the z-position by the movement of position controller with computer 1, and the SF ink inside vat was also refreshed.

Computer 2 was used to run a DLP projector that projected pattern images for photocrosslinking. All pattern images were irradiated onto SF ink surfaces using ArtSage program. ArtSage program treated the area as black except for pattern images. Therefore, by using this program, the light was accurately irradiated only to the area where the light was irradiated. In addition, this program could change the pattern images according to time using a slideshow function. Since ArtSage was the most appropriate program to project pattern images on the surface of SF ink for an accurate period of time, it was used consistently for all experiments.

Before starting 3D printing, the operating system time of computer 1 and computer 2 was synchronized in advance, so 3D printing was performed by matching the start time of programs on computer 1 and computer 2. LabVIEW-based and Autohotkey-based programs on the computer 1 and ArtSage program on computer 2 were run on each computer at the same time. After 3D printing was finished, all programs were automatically closed. The amount of light energy from DLP projector's light source according to brightness of projected image was measured using an accumulated UV meter to confirm the shape of a standard curve. The projected image was black when the gray value was closer to 0, and white when it was close to 255. Amount of the light energy for the brightness of projected images appeared in form of quadratic function (Figure 10).

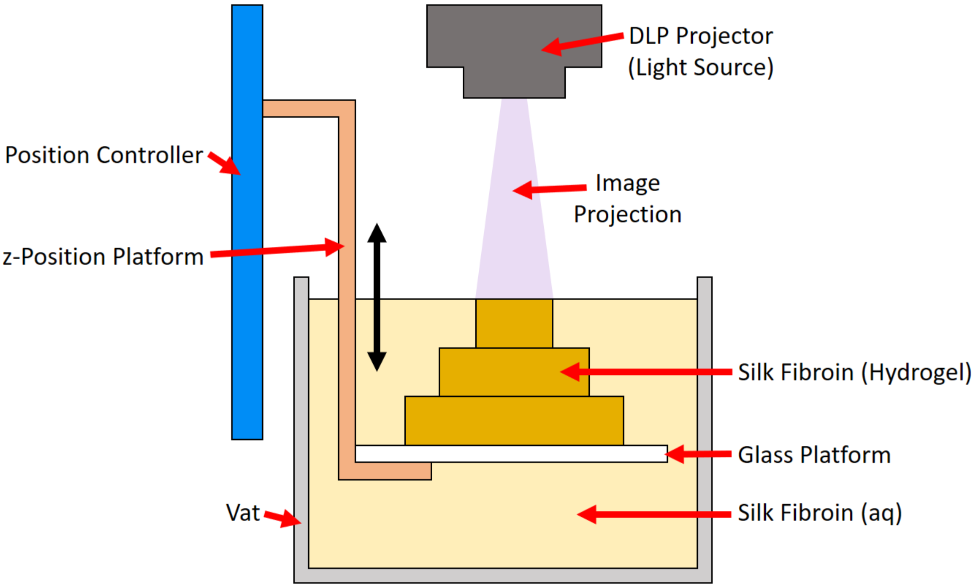

Figure 8. A schematic diagram of a DLP printing system. Control the position controller to change the z-position (Computer 1), and control the DLP projector to project the image (Computer 2). SF hydrogel is fabricated through a photocrosslinking reaction using this system.

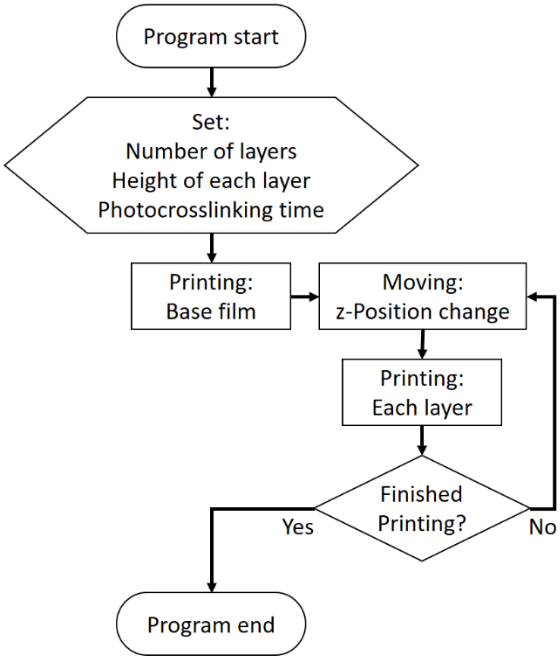

Figure 9. Flow chart of program to operate position controller (Computer 1).

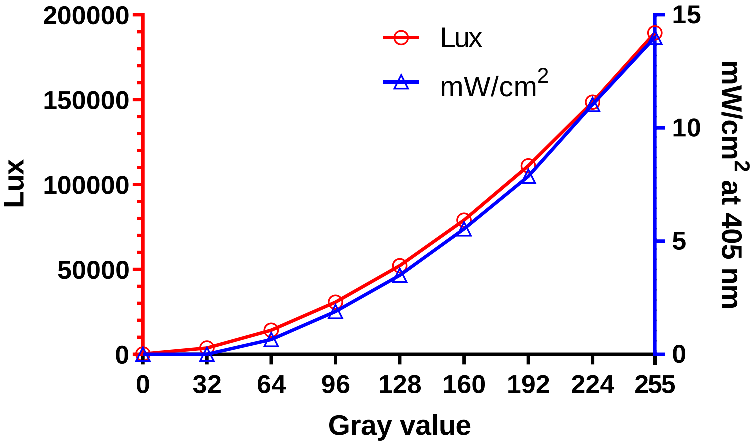

Figure 10. Amount of light energy according to gray value of projected image of light source of DLP projector (Computer 2). The maximum value of light energy varies depending on the performance of the DLP projector, and the light energy curve shows a tendency to increase in a quadratic function as the gray value increases.

3.3. Silk Fibroin-based Microneedles

In previous studies, SF microneedles were often fabricated using negative molds [38, 42, 50, 52, 60, 61]. In the previous research cases, the fabricating method using polymer synthesis requires many processes, and the shape of the microneedle depends on the shape of the mold. Previously reported fabrication methods require many steps, are labor-intensive, and can obtain a simple microneedle structure. In addition, it is difficult to personalize the microneedle structure and obtain a unique shape [62]. However, DLP printing offers the possibility to fabricate 3D microneedles of various shapes by changing the projected pattern images. Depending on how the images are processed, the height and tilt of the microneedle can be adjusted.

SF microneedles were fabricated using DLP printing method using DLP projector with light source in visible light range (Figure 11A). SF hydrogel was obtained by continuously projecting gray-scaled pattern images onto SF/riboflavin solution to induce photocrosslinking reaction of SF. Also, to make smaller structures, a dehydration process is used for hydrogels. First, hydrogels having the same shape as the target structure and different sizes are first prepared. Next, a smaller structure can be obtained by drying-shrinking the hydrogel [63, 64]. Likewise, SF microneedles were made by photocrosslinking SF hydrogel through dehydration process. The dehydration process shrinks the structure of SF hydrogel, and after this process, SF hydrogel turns into sharp SF microneedles. Since SF hydrogel contains about 95% of water and is a soft structure, SF hydrogel must go through dehydration process through drying before it can become SF microneedles.

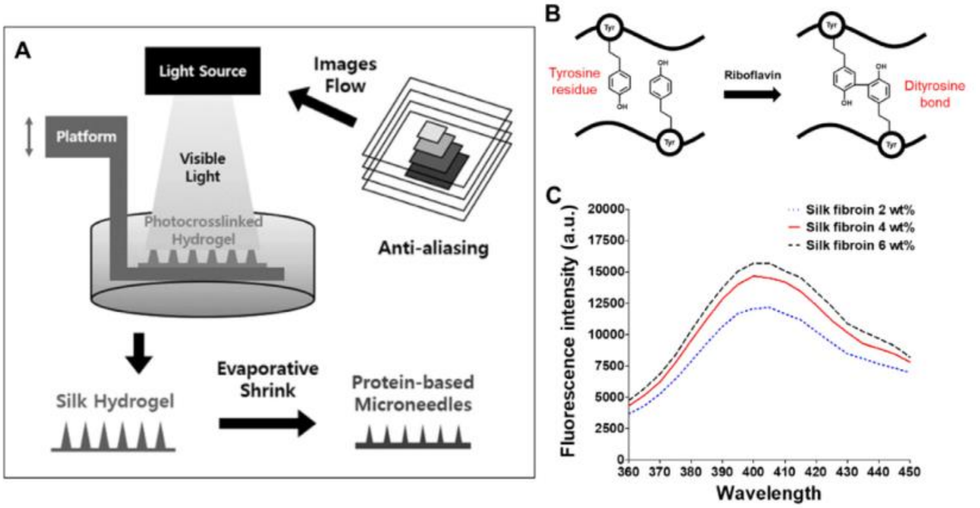

Figure 11. (A) Scheme of DLP 3D printing with SF ink; anti-aliasing was applied to yield microneedles with smooth sides. (B) Formation of dityrosine bonds with riboflavin. (C) Fluorescence intensity from dityrosine bonds at different SF concentrations.

3.3.1. Fluorescence Measurement of Silk Fibroin Hydrogels

DLP printing was performed using photocrosslinking of silk fibroin/riboflavin solution. Here, riboflavin, as photoinitiator, helped form dityrosine bonds by radical reactions between silk fibroin molecules. (Figure 11B) Riboflavin is yellow material that absorbs light in range of 350 to 450 nm to form radicals. Tyrosine, which constitutes part of silk fibroin molecule, is converted into tyrosine radicals by oxygen radicals generated by riboflavin radicals, and tyrosine radicals cause photocrosslinking reaction to form dityrosine bonds. Dityrosine bonding in SF hydrogels formed by photocrosslinking is confirmed by fluorescence light of 400-410 nm excited by light at 310 nm. (Figure 11C) As the fluorescence intensity of dityrosine bonds increases with concentration of SF ink, fluorescence intensity may appear relatively high when a high concentration of SF ink is used.

3.3.2. Fabrication of Silk Fibroin Microneedles

The size of SF microneedle structure depends on the resolution and brightness of DLP projector used in DLP printing process. In DLP printing process, high-resolution projector is mainly used as light source that causes photocrosslinking. Normally, light from the light source is reflected off a series of small mirrors (DLP chips). At this time, each mirror covers one-pixel area. Therefore, image projected on glass platform is bitmap image in which pixels are arranged consecutively. In DLP printing process, the size of a projected image is important because the area of ink that is illuminated causes photocrosslinking reaction. The DLP projector used in the experiment had a width per pixel of about 48 micrometers at its shortest focal length.

Therefore, square images ranging in size from 1 x 1 pixel to 10 x 10 pixels were projected (Figure 12A) to form SF hydrogels, and actual size of the formed hydrogels was measured. At this time, more than 2 minutes of photocrosslinking time was required to form SF hydrogel. (Figure 12B) However, SF hydrogels with a size equivalent to 1 x 1 pixel were not formed even under the condition of photocrosslinking time of more than 10 minutes. This occurred because energy density in the area where light is projected was low, so hydrogel could not be formed [28]. In addition, when SF hydrogel was already formed after 2 minutes or longer of photocrosslinking, SF hydrogel was formed with a larger size than original projected image size.

To confirm boundary formation according to light intensity, 9-level images were created according to grayscale intensity from black to white. The brightest intensity defined 1.0 and darkest intensity defined 0.0. To compare the formation of SF hydrogels under relative light intensities, a small square with bright intensity of 1.0 was placed in center of projection image (Figure 13A). Light energy per area increased as grayscale intensity was closer to the brighter side. An increasing trend was observed as following quadratic function (Figure 13B). This is because DLP projector light sources inherently have luminous intensity growth trend similar to quadratic function as grayscale intensity becomes brighter (Figure 13C-E).

In order to make microneedles with oblique plane through anti-aliasing processing, inverse function of quadratic function was calculated and grayscale was applied to pattern image. If inverse function is obtained through same experimental procedure for all projectors and polymers, anti-aliasing processing can be applied to pattern image. At this time, area treated with anti-aliasing forms SF hydrogel with area smaller than 1 x 1 pixel. For example, if area receiving light at intensity of 0.75 is placed on periphery of region receiving light at intensity of 1.0, SF hydrogel with an area of about 67% of 1 x 1 pixel is formed. In addition, if area receiving light with intensity of 0.25 is placed nearby, hydrogel with area of about 25% is formed. Using this, pattern images for forming hydrogels with smooth slopes were produced for layers 1 to 1000.

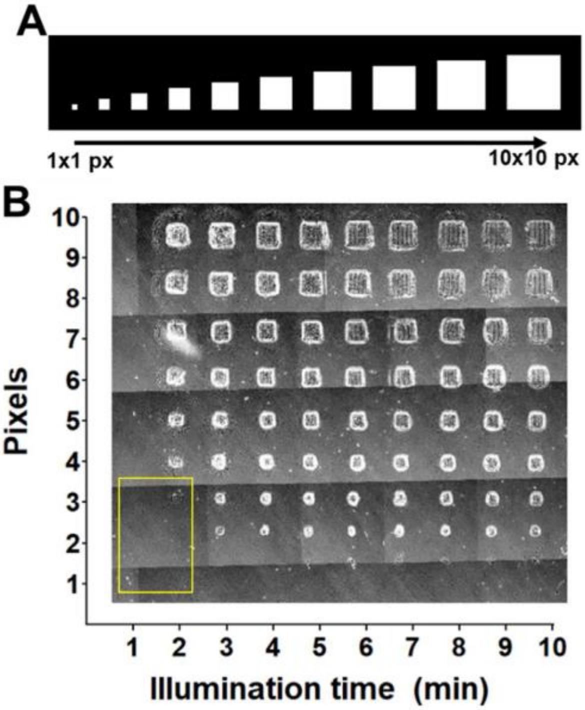

Figure 12. (A) Relative size of the projection images and (B) single-layer SF hydrogels printed at different projection sizes (Pixel dependent test) and illumination times (Time dependent test). (Yellow area: No hydrogel is formed.)

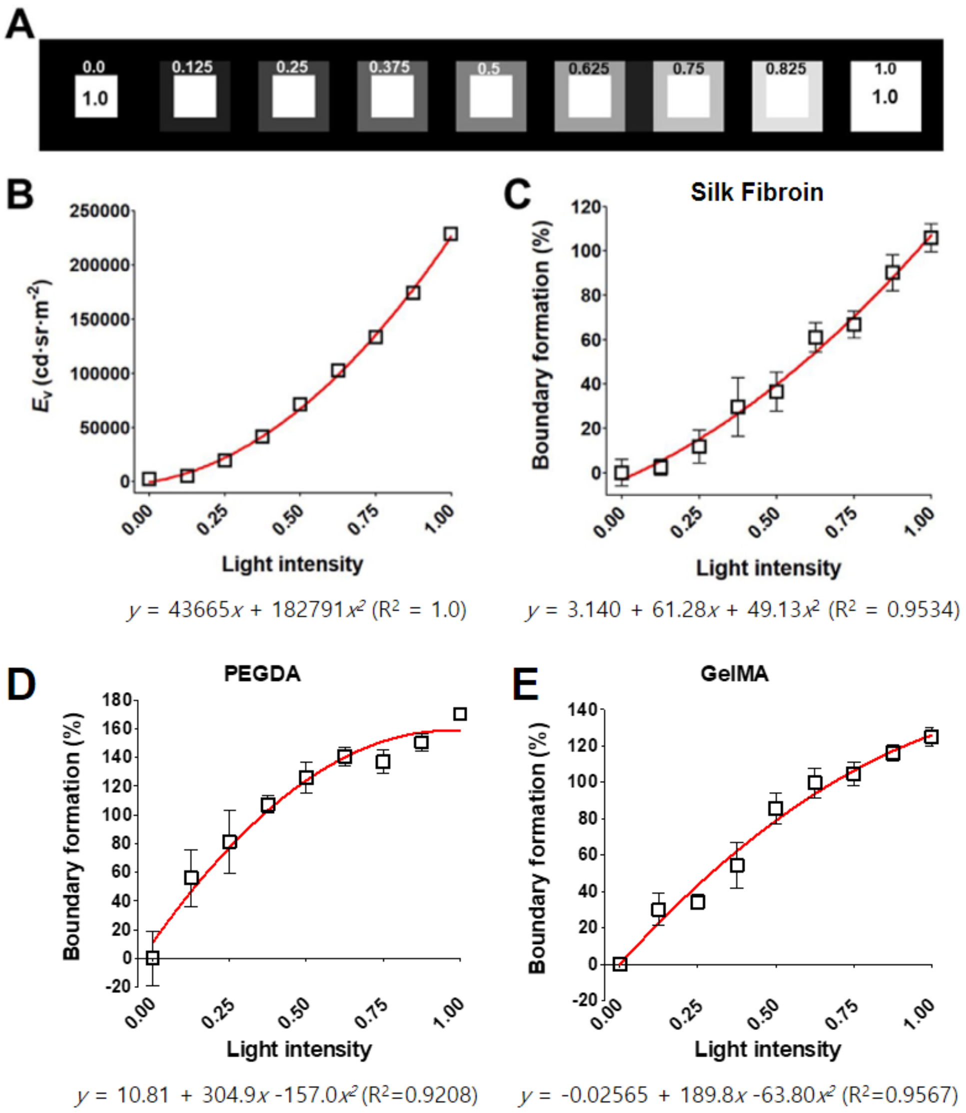

Figure 13. (A) Grayscale applied to measure the size of a hydrogel formed around a small square. (B) Intensity of the light source was controlled according to degree of grayscale, and luminous flux per unit area was measured accordingly. Measurement of boundary formation of the plateau width according to light intensity during production of a columnar (C) SF, (D) PEGDA, and (E) GelMA hydrogel.

Figure 14 is a flow chart of a program that forms pattern images with grayscale applied. Before starting a program, enter the size of microneedle array, total height of microneedles, total number of layers, and boundary formation function obtained in previous process into program. The program repeats as many layers as number of layers to form pattern image. First, fill the entire image with white to have grayscale intensity of 1.0. Then, pattern image is modified by applying grayscale value suitable for position of the layer to edge area. At this time, a correction value is obtained through the boundary formation function. After editing the pattern image, save it as an image file. When the creation of pattern images for all layers is completed, program is terminated.

3.3.3. Morphological Properties of Silk Fibroin Microneedles

Since the structure to be fabricated is microneedle, area of light irradiated to ink decreases as it moves from glass platform to the top. (Figure 15A and B) The tip of SF microneedle structure becomes sharper as uppermost width of hydrogel becomes narrower. In the previous experiment, SF hydrogel was not formed in pixel area of 1 x 1 size, so minimum unit area corresponding to the tip of microneedle was fixed to pixel area of 2 x 2 size. In addition, to form sharp structure, area corresponding to the base of microneedle was fixed as 6 x 6 pixel area. At this time, when layer height is 10 micrometers and total number of layers is 100, SF hydrogel with total hydrogel height of 1000 micrometers was formed. Also, the width of uppermost hydrogel was formed to be about 90 micrometers. (Figure 15C) At this time, when experimental conditions were changed and minimum unit area was fixed to pixel area of 1 x 1 size, height of entire hydrogel was lower than 1000 micrometers. Interestingly, even under altered conditions, width of uppermost hydrogel was about 90 micrometers. This result shows again that minimum unit area to form SF hydrogels in previous experiment is 2 x 2 pixel area.

When silk fibroin hydrogel becomes silk fibroin microneedle through

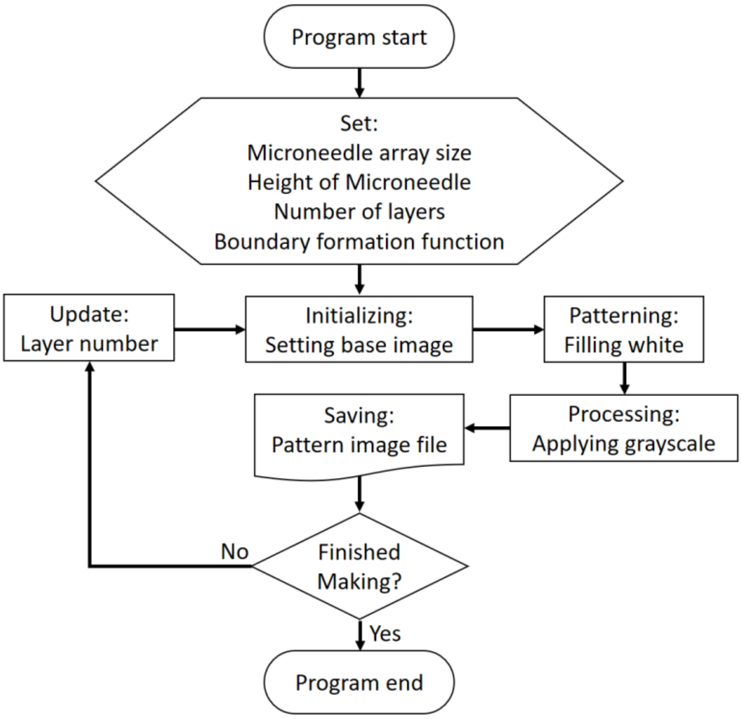

Figure 14. Flowchart of program for grayscale processing of pattern images.

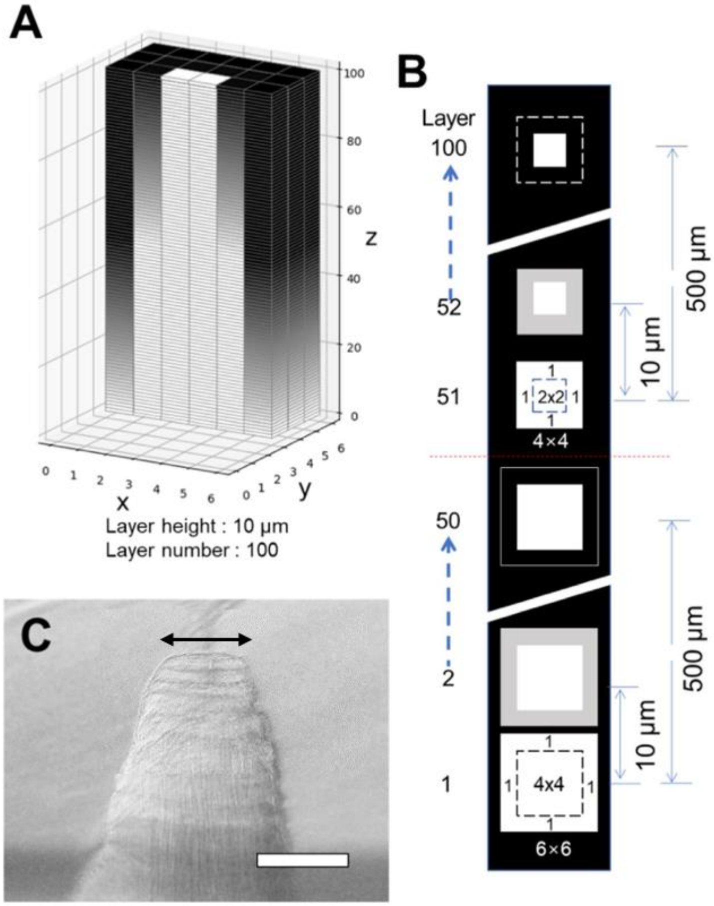

Figure 15. (A) Z-stacked images with 10 mm layer height. (B) Scheme of grayscale application (1 pixel for each side) at the boundary of square patterns (4 x 4 and 2 x 2 pixels). (C) SF microneedle printed to have a base of 6 x 6 pixels and a plateau of 2 x 2 pixels; the scale bar is 100 μm.

drying process, deformation of structure was observed during dehydration. In drying shrinkage process, deformation occurs in horizontal (x-y) and vertical (z) directions of SF structure. Structures with varying heights per layer were fabricated to see if height per layer could affect deformation of structure. When the height of entire hydrogel is same, lower the height per layer, that is, the greater total number of layers, the higher total photocrosslinking time of the entire structure. SF microneedles were fabricated by setting the height of each layer to 10, 25, and 50 micrometers, and height of entire hydrogel to 1000 micrometers.

As a result of measuring direction shrinkage, deformation in x-y direction did not correlate with height per layer. (Figure 16A) On the other hand, in z-direction deformation, the lower height per layer, the lower the shrinkage rate. (Figure 16B) This is because the degree of crosslinking of hydrogel increases as the total number of layers increases and total photocrosslinking time increases when total height of hydrogel is same. Therefore, the lower the height per layer, the higher degree of crosslinking of hydrogel, so the lower shrinkage rate of hydrogel.

Figure 17A shows cross-sections of z-stack images. Upper part in SF hydrogel (Figure 17B) maintained its shape even in SF microneedle after drying (Figure 17C). Due to horizontal shrinkage of hydrogel, SF hydrogel structure becomes sharp microneedle after drying. SF hydrogel structures can be processed into arrays in which several microneedles are continuously arranged when prepared at certain distance (Figure 17D and E).

Since human and animal skin is curved, the flexibility of microneedle array is an advantage. In this study, to observe the flexibility of SF microneedle array, microneedle array was fabricated on PET film and separated. SF microneedle arrays were easily deformed by twisting, infold/outfold bending. (Figure 18) In addition, SF microneedle array could be fabricated on the surface of PVC, aluminum foil, and cellophane tape in addition to glass platform. (Figure 19) This suggests that no special platform conditions are

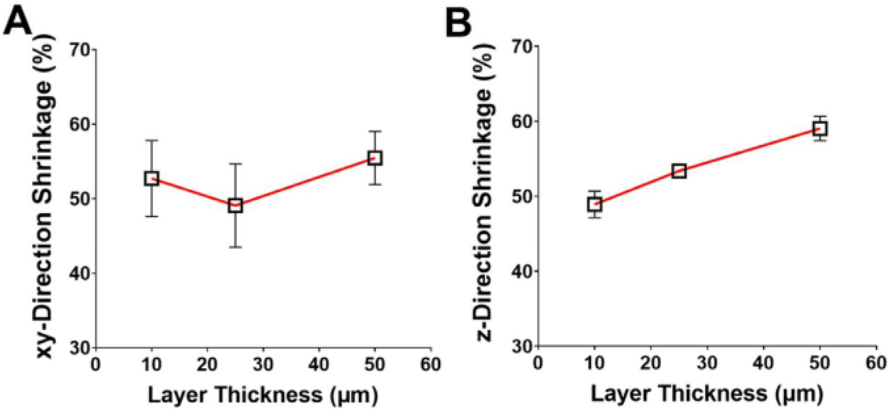

$$\text{Direction Shrinkage (\%)} = \frac{\text{Length}_{\text{wet}} - \text{Length}_{\text{dry}}}{\text{Length}_{\text{wet}}} \times 100$$

Figure 16. Directional shrinkage of hydrogels at different printing layer thicknesses: (A) x-y direction and (B) z direction.

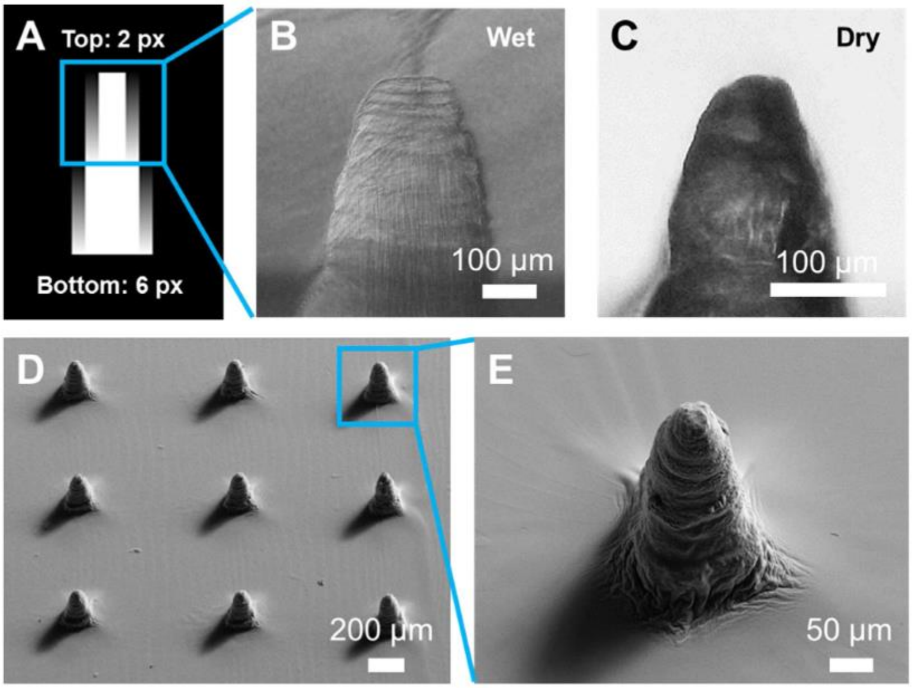

Figure 17. Fabrication of SF microneedles. (A) Z-stacked images of the cross-sectional microneedle structure. Photographs of a printed microneedle tip (B) before and (C) after drying; the scale bar is 100 μm. (D) FESEM image of the microneedle array; the scale bar is 200 μm. (E) Magnified view of a single microneedle; the scale bar is 50 μm.

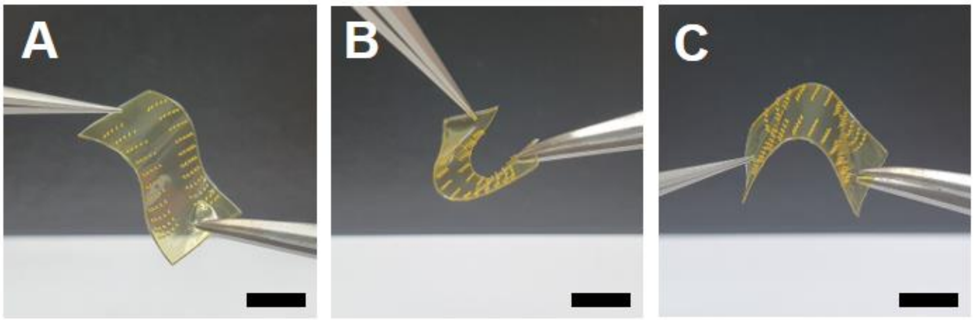

Figure 18. Flexibility test. (A: Twist, B: Infold and C: Outfold test); the scale bar is 10 mm.

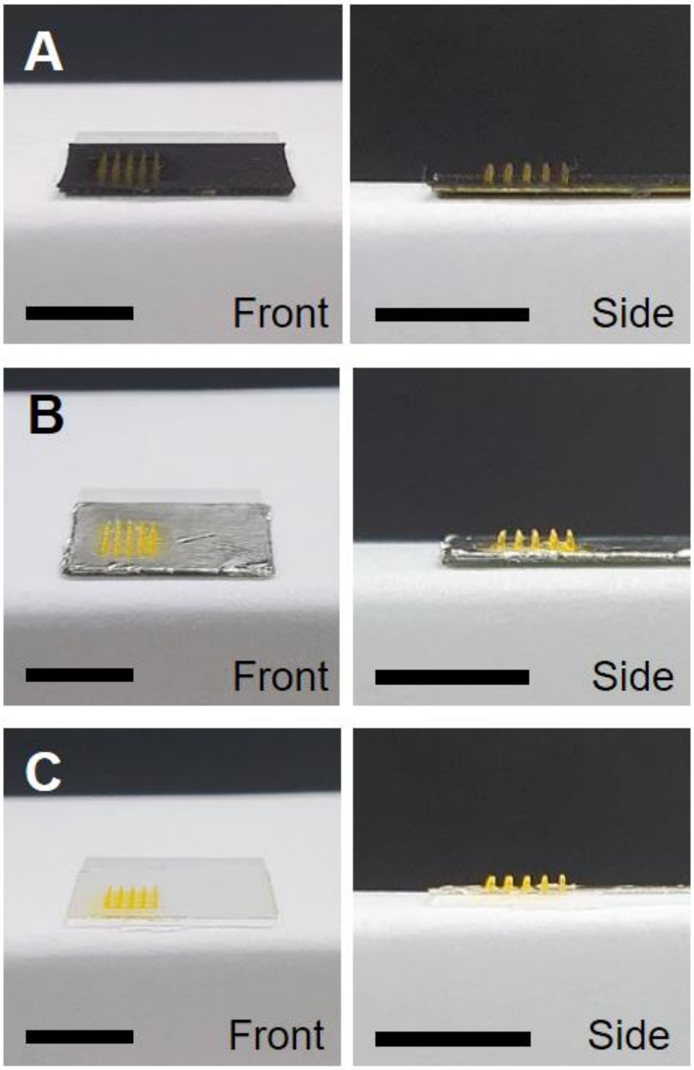

Figure 19. Printing on various surfaces. (A) PVC, (B) Aluminum, (C) Cellophane.; the scale bar is 5 mm.

required to use SF as 3D printing ink.

3.3.4. Mechanical Properties of Silk Fibroin Microneedle

The microneedles must maintain their shape while penetrating the skin. The UTM compression test was performed to ensure that silk fibroin microneedles maintained their shape while being subjected to force. After the compression test, no significant damage to the shape of the microneedle was observed (Figure 20A). This means that SF microneedle could penetrate the skin. During the compression test, a single SF microneedle was gradually compressed up to 100 micrometers, and compressive strength showed a linear increase up to 1000 mN or more (Figure 20B).

3.3.5. Penetration Test of Silk Fibroin Microneedles on Porcine Skin

Finally, the feasibility of SF microneedles as drug delivery carriers was checked. The tip area of the SF microneedle was coated with Rhodamine B solution, and a penetration test was performed on cadaver pig skin. SF microneedles successfully penetrated pig skin and formed needle marks visible to the naked eye on the pig skin surface. (Figure 21) Since the thickness of stratum corneum of skin is less than about 20 micrometers, SF microneedles can sufficiently reach the epidermis. When pig skin was irradiated with UV light, rhodamine B fluorescence was observed, confirming that SF microneedles can be used as drug delivery carriers.

Transdermal delivery of rhodamine B coated on surface of SF microneedle to pig skin after penetration test was observed through cross-sectional imaging of pig skin. First, stratum corneum on the skin surface was stained with FITC. Since thickness of epidermis is about 100 micrometers, depth to which point rhodamine B, shown in Figure 22, reached in pig skin was checked using fluorescence microscope. SF microneedle penetrated pig skin up to about 200 micrometers, confirming the possibility of efficient drug delivery [65, 66]. In the case of silk films without microneedles, rhodamine

B only reaches stratum corneum, making it difficult to use them as drug delivery carriers. In other words, SF microneedles fabricated by DLP printing are promising tools for transdermal drug delivery systems.

3.3.6. Limitations of Measurement Method

Since the purpose of the microneedle is to make a device for transdermal drug delivery, it is necessary to compare how the drug delivery efficiency appears as a drug delivery system. In general, the cumulative amount of a drug or fluorescent substance over time is measured and compared [47, 62, 67, 68]. In this study, an attempt was made to fabricate and measure a microneedle with a fluorescent material embedded on SF hydrogel, and a SF microneedle coated with a fluorescent material was performed. First, when the fluorescent material was supported on the SF hydrogel, the fluorescent material did not diffuse into the pig skin. This is assumed to happen because there is not enough space for the fluorescent material to come out of the shrunken SF. Next, when measured in a coated state, it was impossible to measure the fluorescent material itself (when pig skin was used) or the intensity of the fluorescent material to be measured was not constant (when using a transparent hydrogel). Because of this, it was not possible to obtain a graph of cumulative amount over time. It was difficult to secure a constant distance value to measure the amount of fluorescent material separated from the coated fluorescent material. Therefore, this study tried to show that the material was clearly transferred indirectly using the penetration test (Figure 21) and fluorescence image (Figure 22).

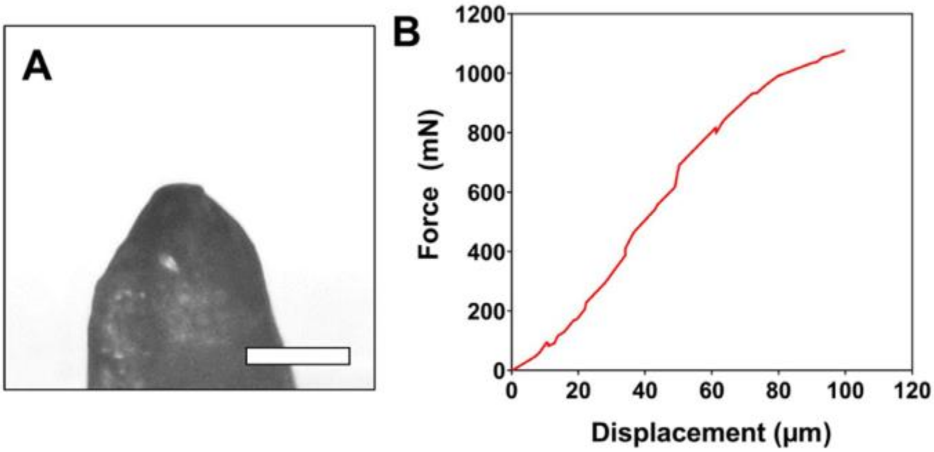

Figure 20. Compression test of a single microneedle. (A) Optical microscopy image of a microneedle after the compression test; the scale bar is 100 μm. (B) Force-displacement curve of a microneedle.

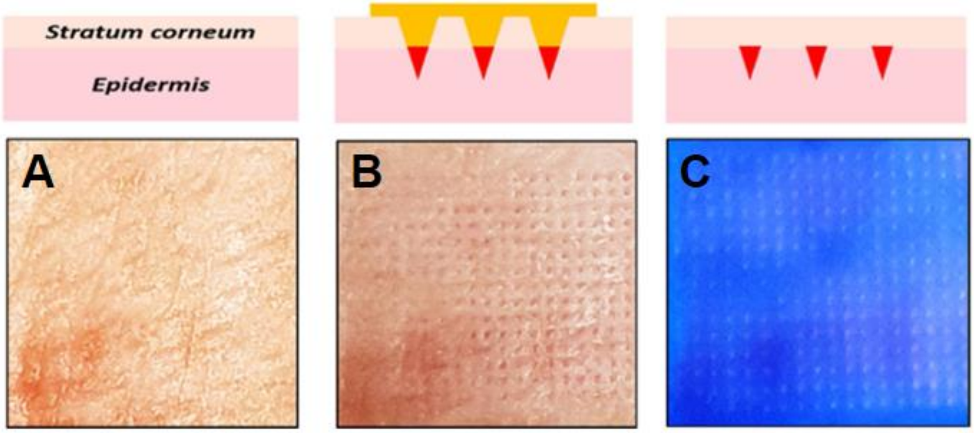

Figure 21. Photographs of the microneedle penetration test with cadaver pig skin. (A) Flexible SF microneedles coated with rhodamine B solution (0.01 wt%) for 10 min and then injected into pig skin for 10 min to deliver rhodamine B. (B) Pig skin before penetration and (C) after penetration of the microneedles. (C) Rhodamine B in pig skin observed under UV illumination.

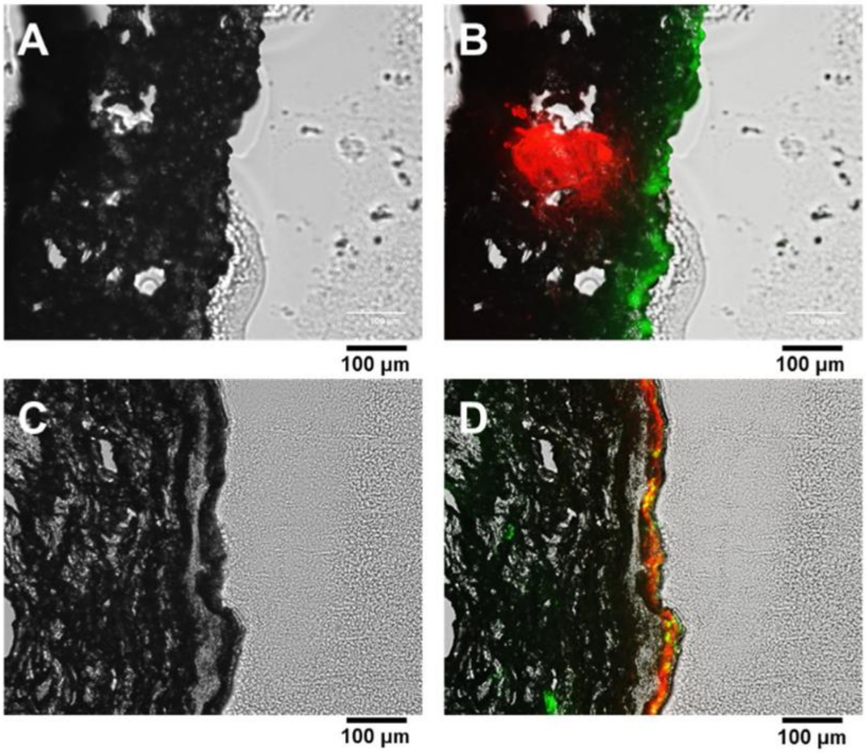

Figure 22. Fluorescence microscopic images of skin sections after the penetration test with rhodamine B. (A) Phase contrast and (B) fluorescence images of a skin section after the delivery with a SF microneedle. (C) Phase contrast and (D) fluorescence images of a skin section after the delivery with a control flat SF film. SF microneedles and the control SF flat surface were coated with rhodamine B, and the skin surface was coated with FITC.

3.4. Silk Fibroin-based Optical Film for Light Harvesting

Solar energy is the most abundant renewable energy, giving life to all life on Earth. Nature created the process of photosynthesis to convert sunlight energy into chemical energy. Humans have developed photovoltaic cells for light harvesting to generate electrical energy [69, 70]. Light harvesting is the process by which a photovoltaic device uses incident light to produce electrical energy. In order to increase energy conversion efficiency, various researches are being conducted on semiconductor materials, thin films, and substrates. Methods using light diffraction are also being actively researched. For example, there are methods using the diffraction and scattering characteristics of materials [57], and methods of making a grating using nanopatterns and then placing them on the edge to diffract light on blind spot of the photovoltaic device to the photovoltaic cell [56] (Figure 23).

As a natural polymer material, SF has sustainability, biodegradability, and environmental friendliness. SF can also be processed in solution [57]. Glass or plastic substrates are usually used as materials for fabricating photovoltaic devices, and the reason for this is the material's mechanical strength and optical transparency. The possibility of using SF as a substrate material by replacing existing glass and plastic has been reported [71]. SF can be patterned through various methods. In this study, SF-based optical film was fabricated using DLP printing, and after confirming the light diffraction property, light harvesting ability was simply evaluated.

3.4.1. Fabrication of Silk Fibroin Optical Film for Light Harvesting

Photocrosslinking time for the pattern formation on SF film was investigated. Through printing fidelity evaluation, appropriate light irradiation time for pattern printing was determined. A glass platform was used as a printing platform. 20 vertical stripe patterns formed at different light irradiation times, and the appropriate light irradiation time was determined at 1 min intervals in the range of 1 to 20 min. (Figure 24)

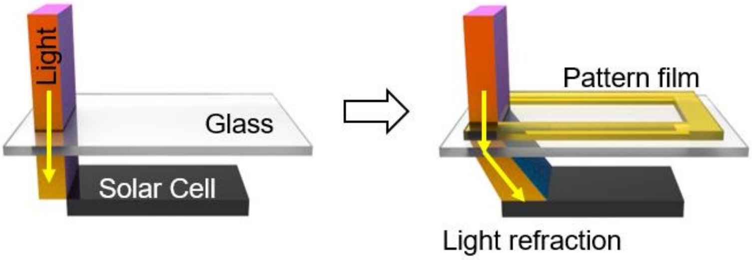

Figure 23. Scheme in which a patterned SF optical film contributes to the power generation efficiency of a photovoltaic cell. By diffracting sunlight that does not reach the solar cell, it helps the photovoltaic cell to produce more energy.

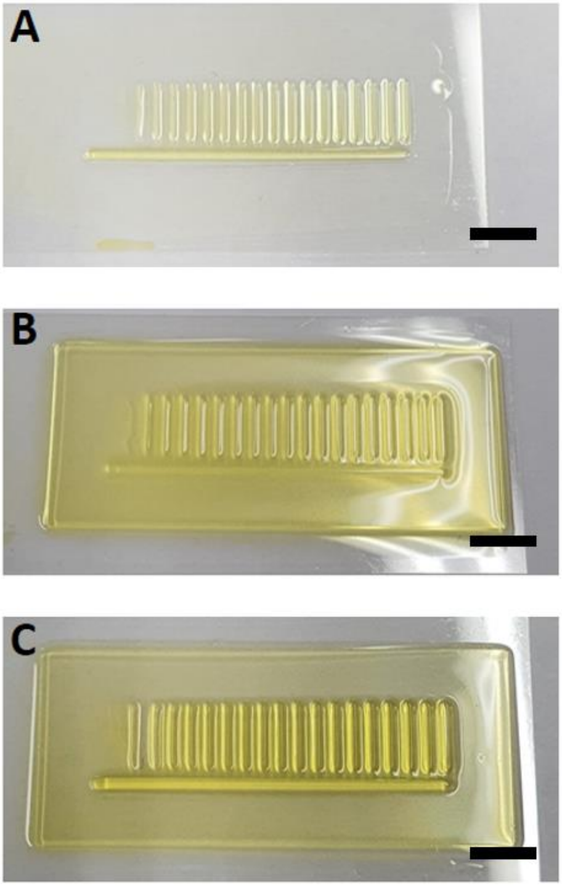

Figure 24. (A) Formation of SF hydrogel directly on the glass platform. (B) Formation of SF Hydrogel with a thickness of 200 μm on base SF hydrogel formed by irradiation with light for 15 minutes. (C) Formation of SF hydrogel with thickness of 400 μm on base SF hydrogel formed by light irradiation for 15 minutes. (SF 4 wt%, Riboflavin 0.5 mM); the scale bar is 5 mm.

First, SF hydrogels were printed directly onto glass platform. On glass platform, a hydrogel became a film, which was a base layer of patterns to be printed. Therefore, experiment was conducted to find appropriate time to print hydrogel to be base film. SF hydrogel began to form in shape of stripes under condition of light irradiation time more than 10 min (Figure 25A). Next, time to print patterned hydrogels on the base film was determined. z-Position height for printing pattern was set to 200 and 400 micrometers. SF hydrogels began to form in shape of stripe even under conditions of 200 and 400 micrometers when the light irradiation time was longer than 10 min (Figure 25B and C). Therefore, for the stable formation of a base film and a patterned film, the photocrosslinking time per layer was set to 15 min.

3.4.2. Refractive Index of Silk Fibroin Optical Film

Refraction is the change in the speed of wave as it passes from one medium to another, changing its path at the interface. Different materials have their own absolute refractive index values. In case of polymers, the value of refractive index tends to converge to a specific value as polymerization reaction progresses [72-74]. In this study, three methods were used to confirm whether value the of refractive index of SF changes as the polymerization reaction proceeds. Firstly, the relationship between photocrosslinking time and refractive index of SF film was examined. It would determine the effect of fabrication process of a SF film on the refractive index. Secondly, the relationship between the mass concentration and the refractive index of a SF film was examined. Lastly, the relationship between the SF film thickness and the refractive index of a SF film was examined.

When preparing hydrogel, the photocrosslinking time was set at 5 min intervals from 5 to 20 min, and SF films were prepared to check the refractive index (Figure 26). As the photocrosslinking time increased, the refractive index of SF film decreased from approximately 1.556 at 5 min to approximately 1.550 at 20 min. It was not possible to confirm that the refractive index converged to a specific value while the photocrosslinking time increased to 20 min. However, the decreasing trend was clear to consider that the refractive index of a pristine silk film without any treatment was about 1.53 [72]. It can be expected that the refractive index converges to some value above about 1.53 as photocrosslinking time increases.

There was no difference in refractive index depending on the mass concentration of SF aqueous solution used to print hydrogel. In the refractive index data according to the photocrosslinking time, the mass concentration of SF aqueous solution did not have significant effect on the refractive index under the same photocrosslinking time. In addition, the similar trend was observed for the refractive index of SF film while the photocrosslinking time was increased to 20 min. Therefore, the mass concentration of SF aqueous solution is not related to the refractive index of SF films.

There was no relationship between thickness and the refractive index of SF film. When the first layer hydrogel was printed to form a base film structure on glass platform, it was difficult to precisely control the thickness of the base film because the z-position of glass platform could not be accurately set. Therefore, the thickness of base film might vary every fabrication. Films were prepared several times under conditions of 15 min light irradiation time and the refractive index was measured. According to data of film thickness and refractive index, the refractive index values were similarly measured regardless of thickness. Also, the mass concentration of SF aqueous solution and the thickness of SF film were not related.

In conclusion, the main factor affecting the refractive index of SF film was the photocrosslinking time to fabricate a SF hydrogel. In order to fix refractive index of film in subsequent experiments, photocrosslinking time was fixed at 15 min.

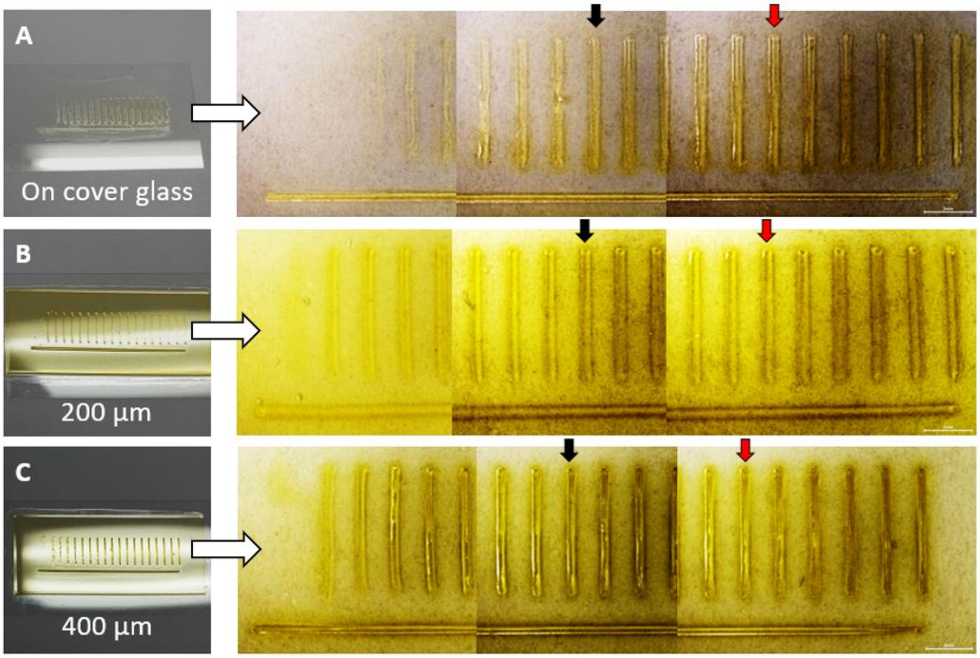

Figure 25. Printing fidelity evaluation. SF hydrogel was fabricated (A) on cover glass, (B) with a thickness of 200 µm, and (C) 400 µm on the base SF hydrogel. Intended shape appeared when photocrosslinked for more than 10 minutes. (Black mark) Appropriate shape was achieved when photocrosslinked for more than 15 minutes. (Red mark)

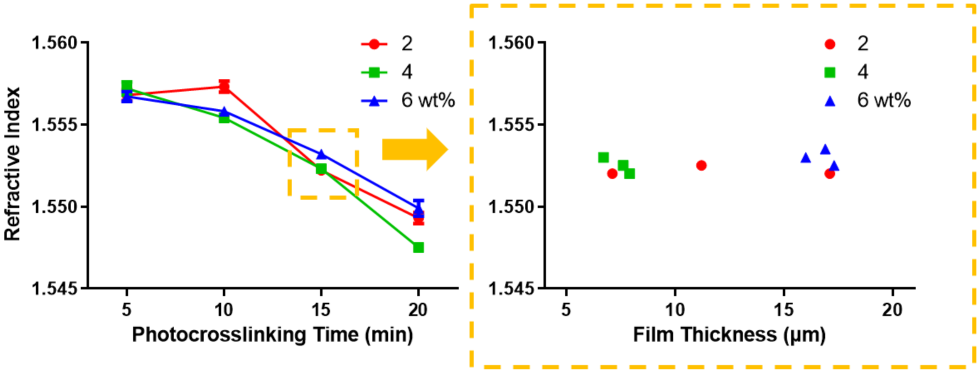

Figure 26. Results of refractive index measurement of SF films fabricated under various conditions.

3.4.3. Various Pattern Formation on Silk Fibroin Optical Film

In order to determine appropriate shape of pattern to be printed on base film, SF film was produced by projecting various shapes of pattern images. (Figure 27A and B) First, in case of basic shape pattern with pattern image of about 9 px thickness, pattern structure with clear shape and height was created. On the other hand, in case of basic shape pattern with pattern image of about 1 px thickness, marks similar to pattern image were observed on base film, but height of structure was not clear. Since light intensity may vary depending on type of DLP projector used in experiment, there is minimum response pixel thickness depending on experimental environment. This is because SF hydrogels cannot be formed if light energy is insufficient.

Therefore, it was necessary to find an appropriate thickness for the pattern. Pattern image with 1, 2, 3, 4, and 5 px thickness mosaic pattern was created to make the film. (Figure 27C) In 1 and 2 px thickness mosaic pattern area, flat-like results were obtained, but the height of mosaic structures was observed in 3, 4, and 5 px thickness mosaic pattern areas. Therefore, in this experimental environment, the pattern image with a thickness of 3 px or more must be used. Finally, to check the possibility of using the 2 px thickness condition, a stripe pattern image with 2 px thickness and 2 px interval was created and the film was fabricated. (Figure 27D) In this case, there were stripe marks on surface, but there was no actual space between the stripes. Therefore, it was difficult to say that the intended shape was formed, so it was reconfirmed that a pattern image with a thickness of 3 px or more should be used.

3.4.4. Light Diffraction Properties of Silk Fibroin Optical Film

There were limited ways to place pixels in a contiguous manner in a rectangular flat image. Therefore, pattern images were created according to the basic method of arranging pixels, and the diffraction pattern of light was observed according to the pattern. (Figure 28) As shown in Figure 28A when

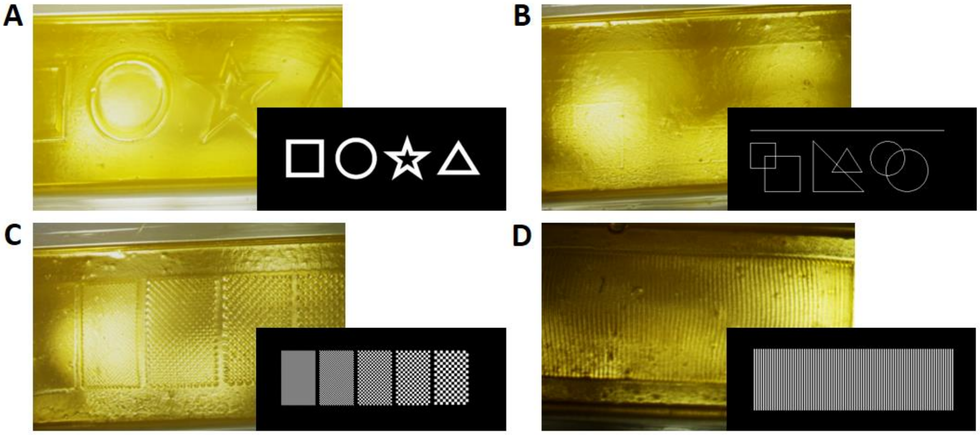

Figure 27. Patterned SF Film. (A and B) Basic shape pattern. (C) Mosaic pattern. (D) Stripe Pattern.

the laser passed through the pattern consisting of one square, the pattern of concentric circles appeared due to diffraction. This is due to the diffraction phenomenon that occurs when light passes through areas with different heights of film. In the case of a pattern in which two or three squares are connected, such as Figure 28B and C, the straight-line diffraction pattern is observed in a direction perpendicular to the direction in which the squares are connected. From this, it can be seen that diffraction will occur in the direction perpendicular to the stripe in the case of a pattern consisting of several squares, that is, a stripe pattern. Similarly, when squares are arranged diagonally, diffraction patterns overlap in the direction perpendicular to the diagonal (Figure 28D and E). In the case of broken diagonal lines, diffraction patterns also appear perpendicular to each other (Figure 28F). Finally, if squares are repeatedly arranged like a mosaic, the overlapping of diffraction patterns is further deepened (Figure 28G and H). In conclusion, the most effective way to diffract light is to utilize straight-line pattern such as stripes. This is the same principle as using diffraction grating manufactured in form of stripes in previous studies [56, 57].

The reason why these patterns appear is that diffraction of light occurs due to the SF film, and the diffracted light repeatedly causes destructive and constructive interference at regular intervals. The length of this regular interval is generally proportional to the wavelength of the light (Young's experiment). It is clear that diffraction caused by the SF film has occurred, simply by the appearance of a diffraction pattern on the screen. But, to obtain clearer evidence, the interval of the patterns was measured at the same distance (about 200 cm) using a red laser (650 nm) and a green laser (528 nm). The interval of the patterns displayed by the red laser was about 5.1 cm, and the spacing of the patterns by the green laser was about 4.1 cm. The ratio of the laser wavelength and the interval of the patterns are similar at 1.231 (=650/528) and 1.243 (=5.1/4.1), respectively (Figure 29). Therefore, it is clear that the pattern displayed on the screen is a diffraction pattern.

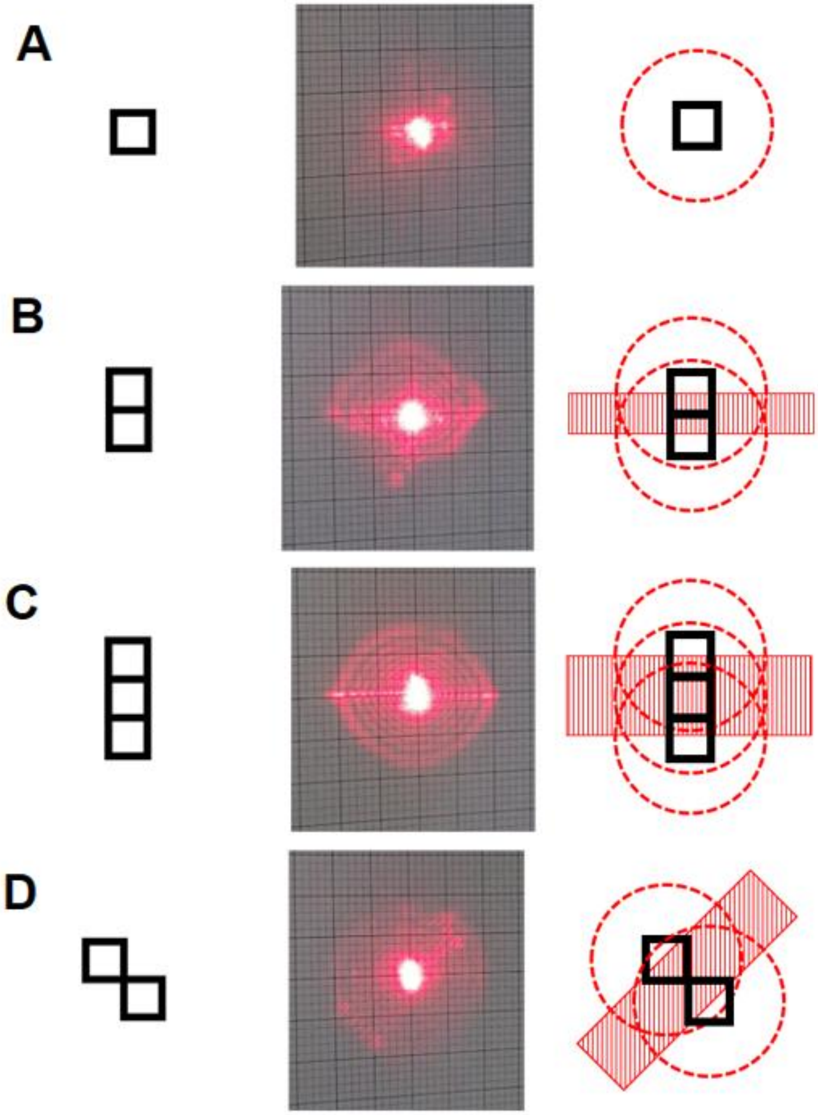

Figure 28. Diffraction overlap pattern of laser light according to arrangement position of square pixels. (A-D)

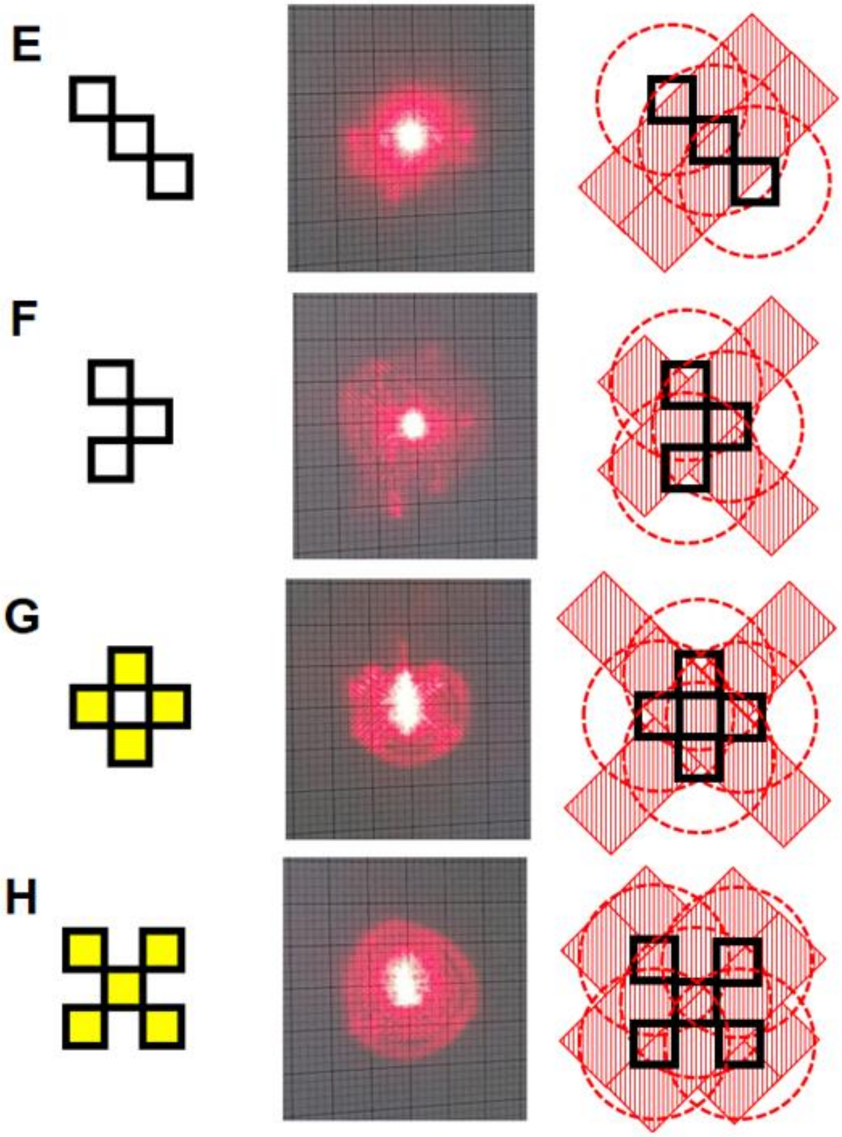

Figure 28. Diffraction overlap pattern of laser light according to arrangement position of square pixels. (E-H)

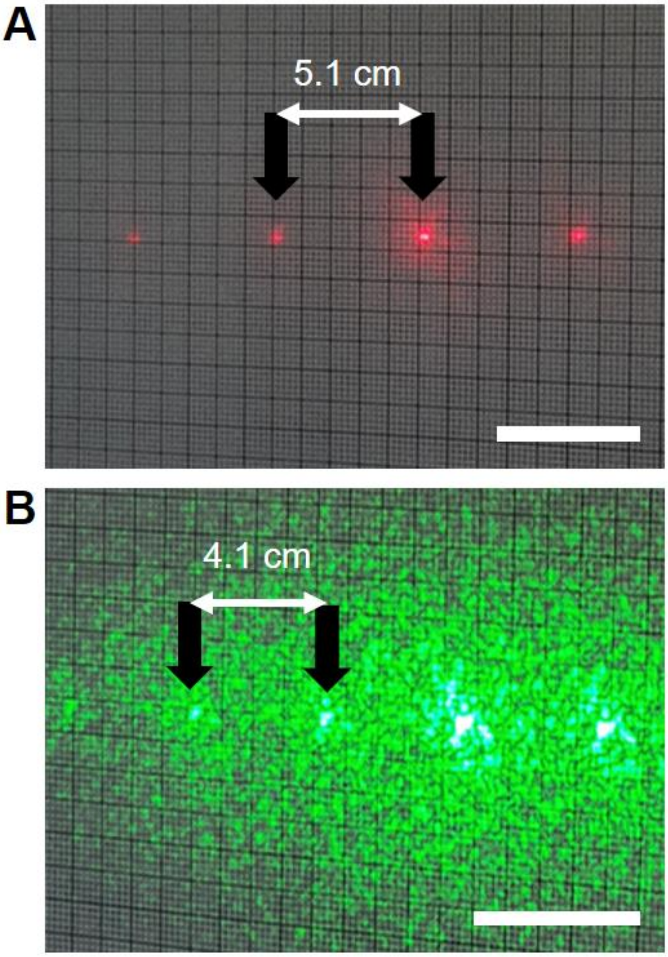

Figure 29. Diffraction patterns for two laser types. (A) The patterns displayed by the red laser (650 nm) and (B) the patterns displayed by the green laser (528 nm).; the scale bar is 5 cm.

3.4.5. Pattern Images for Fabrication of Patterned Silk Fibroin Films

Four types of patterns were created to compare the light diffraction effect and energy generation effect according to a type of pattern imparted to SF film. (Figure 30) First is when the area occupied by a pattern on film is different (Area), the second is when the number of pattern lines is different (Line), the third is when the width of the pattern line is different (Width), and the fourth is when the shape of the pattern is not straight-line (Shape). Pattern images in the case of non-straight lines were produced in form of a sin curve or zigzag. sin Curve and zigzag pattern images were created by a patterning program that outputs repeated pattern images, respectively. When the program starts, the type of pattern, number of repetitions of the pattern, and total length of the pattern are input. When the pattern is formed in the entire image area, the pattern image is saved and the program is terminated. (Figure 31) Then, gray value analysis was conducted for each case, and the diffraction effect of light was measured and compared. In addition, photovoltaic panel voltage analysis was conducted for each case to measure the voltage generation effect of the PV panel.

To proceed with gray value analysis, the experiment was established by referring to previous studies [56]. Film samples were taken with a CCD sensor of a DSLR camera to see shadow areas caused by SF optical film. The brightness of the surrounding environment was fixed at a relatively dark environment of about 240 lux, and after removing the lens of the DSLR, all images were obtained by placing SF optical film in front of the CCD sensor. When the SF optical film was photographed through a CCD sensor, different shadow regions were created depending on the type of film structure. This is because the light is diffracted toward surroundings due to film structure, and therefore light in that area does not directly reach the sensor and was captured as a shadow. For example, as the number of lines in optical film increases, the shadow area also widens (Figure 32). This is because the diffraction effect along each line appeared simultaneously. As can be seen in Figure 32, the

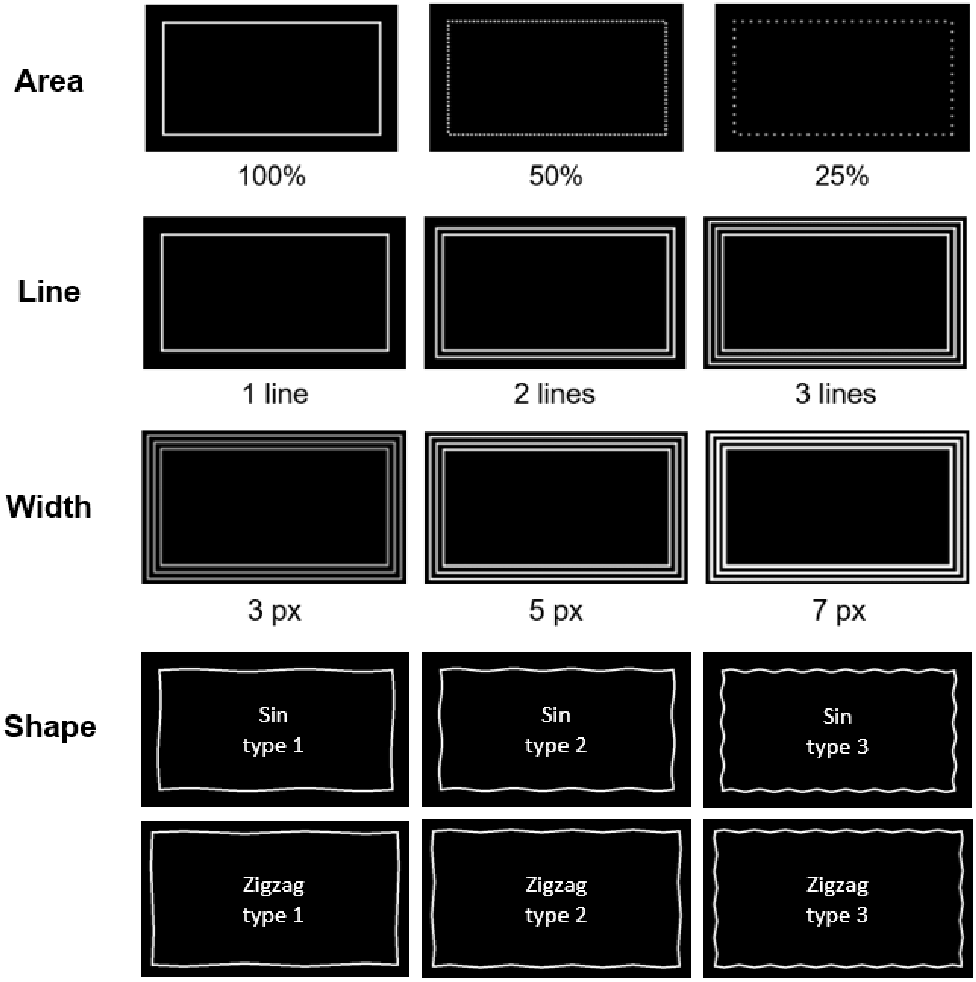

Figure 30. Four types of patterns to compare light diffraction effect and energy generation effect.

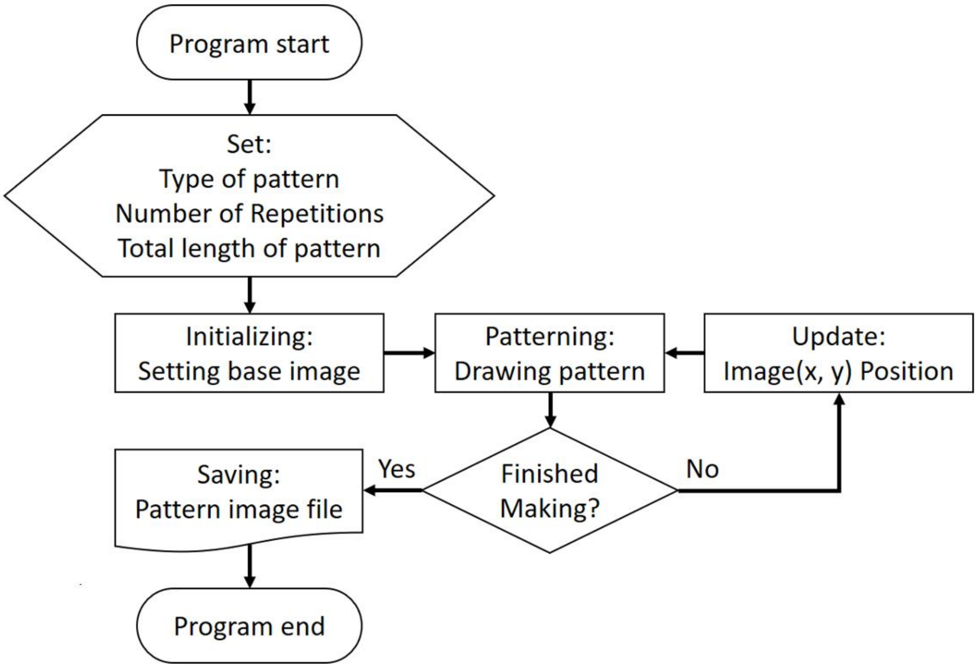

Figure 31. Flowchart of program for making sin curve and zigzag pattern images.

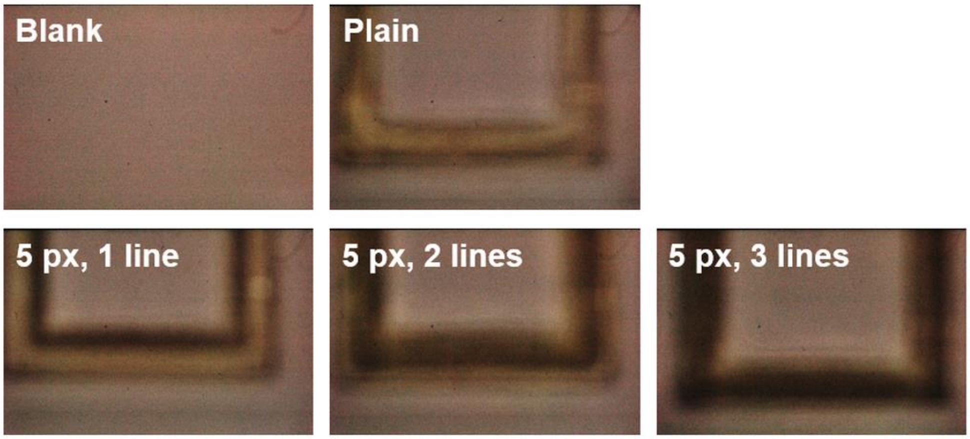

Figure 32. Shadow of SF optical film shooting by CCD sensor. Photographs taken without anything (Blank), SF flims without any patterns (Plain), and SF flims with different numbers of lines (5 px, 1-3 line(s)).

larger number of lines with the same 5 px thickness in the SF optical film structure, the wider shadow area.

3.4.6. Gray Value Analysis of Silk Fibroin Optical Film

In the photograph of the SF optical film taken directly for gray value analysis, it is observed that the shape of the shadow changes according to the pattern of the film (Figure 32). At this time, the brightened area has a higher gray value than before it was brightened. Therefore, by comparing the increase in gray value in this area, the diffraction effect of light according to the pattern can be compared indirectly. Since this experiment requires a shadow, it cannot be conducted in a dark room, and since this measured value may appear differently depending on the type of CCD sensor and ambient brightness, it does not mean an absolute increase in brightness.

Gray value is lower in the state where the cover glass is placed (Glass) and in the state where the Plain sample is placed (Plain) than in the state where there is nothing in front of the CCD sensor (Blank). 5 px, 3 lines, 400 μm sample showed diffraction of light toward photovoltaic due to presence of pattern, which resulted in higher gray value than that of blank (Figure 33). So, the change of gray value according to the area occupied by the pattern was investigated (Figure 34A). The amount of change in gray value was positive only when the pattern area was 100%, and negative when the pattern area was 50% and 25%. This is a clue that the area occupied by the pattern can affect light diffraction. It can also be seen that there is more light diffraction effect when the pattern exists as a continuous line. Therefore, it is necessary to further investigate different kinds of patterns composed of continuous lines. So, the change of gray value according to the number of lines of the pattern and the height of hydrogel when the width is fixed at 5 px was investigated (Figure 34B). Since the layer height of the hydrogel can be set to various values in the process of fabricating the pattern on the SF film, it is important to check whether there is an effect due to the layer height. When the number

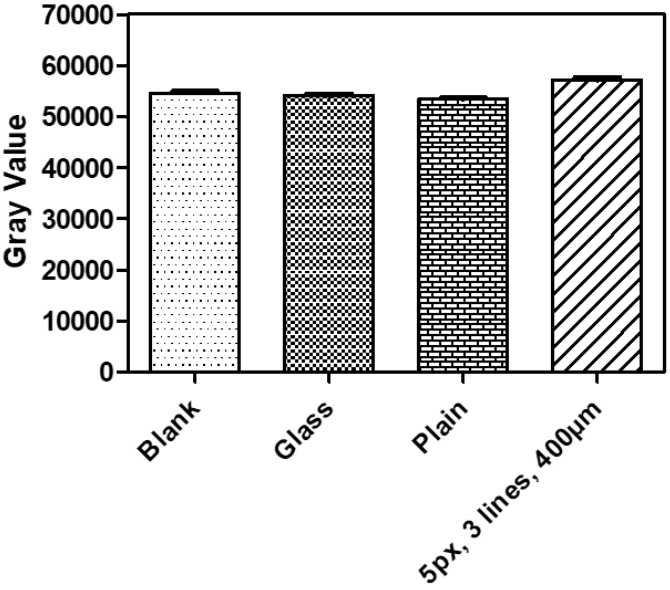

Figure 33. Gray value analysis result for comparison of Blank, Glass, Plain, and 5 px, 3 lines, 400 μm conditions.

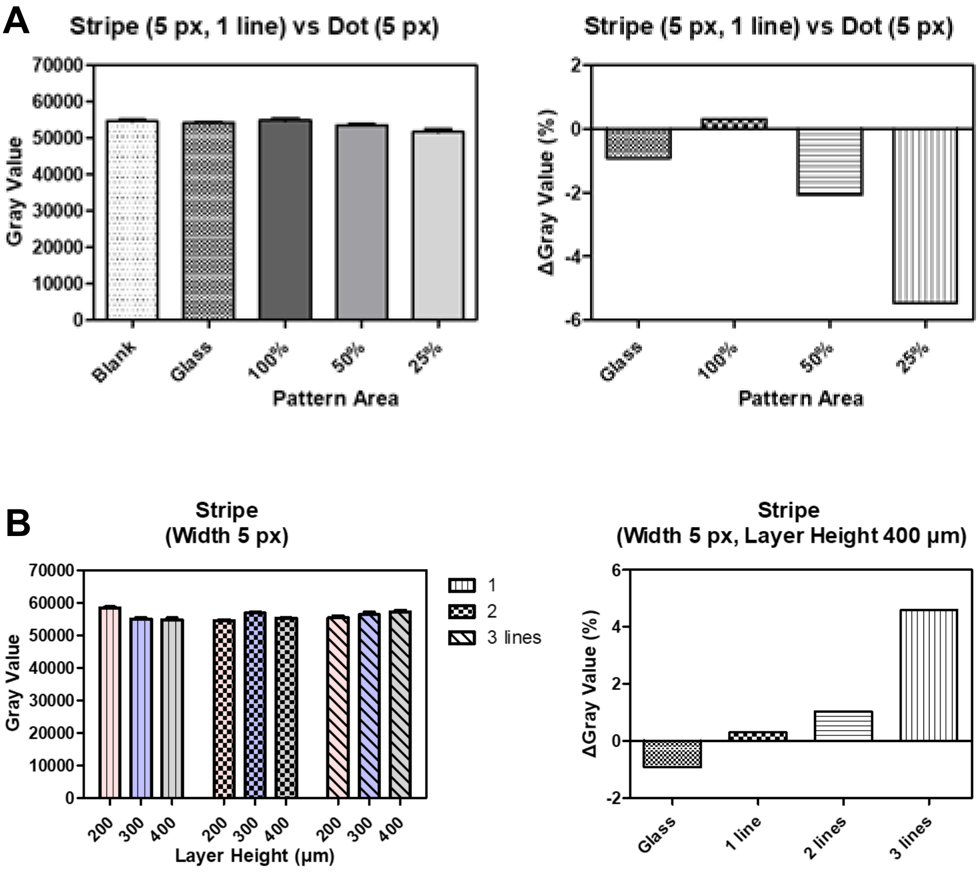

Figure 34. (A) Gray value analysis result and change in gray value (%) for various area of pattern. (The stripe is the pattern with 5 px, 1 line, 400 μm, the dot is the pattern with 400 μm) (B) Gray value analysis result and change in gray value (%) for various number of line of pattern.

of lines was 1 with width fixed at 5 px, the higher the height condition of hydrogel, the lower the gray value. However, it did not decrease compared to the blank condition.

Before drying with SF film, the effect of the size of the pattern made on the SF hydrogel was also investigated. Figure 35 is the relationship between the height condition of hydrogel and the width of the line pattern when patterns are produced. It was observed that the higher the height condition of hydrogel (400 μm), the more the gray value increased. It is inferred that there are the various conditions for the number of lines and layer height to make a pattern film that causes light diffraction, and in this study, 7 px, 3 lines, 400 μm sample showed the best results.

According to linear gray value analysis, the gray value decreases as the number of repetitions of the sin curve pattern increases (Figure 36A). But there were points in an actual where light converges photovoltaic cell. Since the direction of light diffraction is different at each point of the sin curve, it is difficult to discuss with linear analysis. Similarly, the zigzag structure also has light convergence and scattering points in the photovoltaic region (Figure 36B). A change in the value of the gray value appeared, but this does not explain the good or bad when using the sin curve or zigzag pattern. It is difficult to discuss by linear analysis, such as the sin curve structure. In this case, it is effective to investigate the value of the actual voltage generated by the photovoltaic cell.

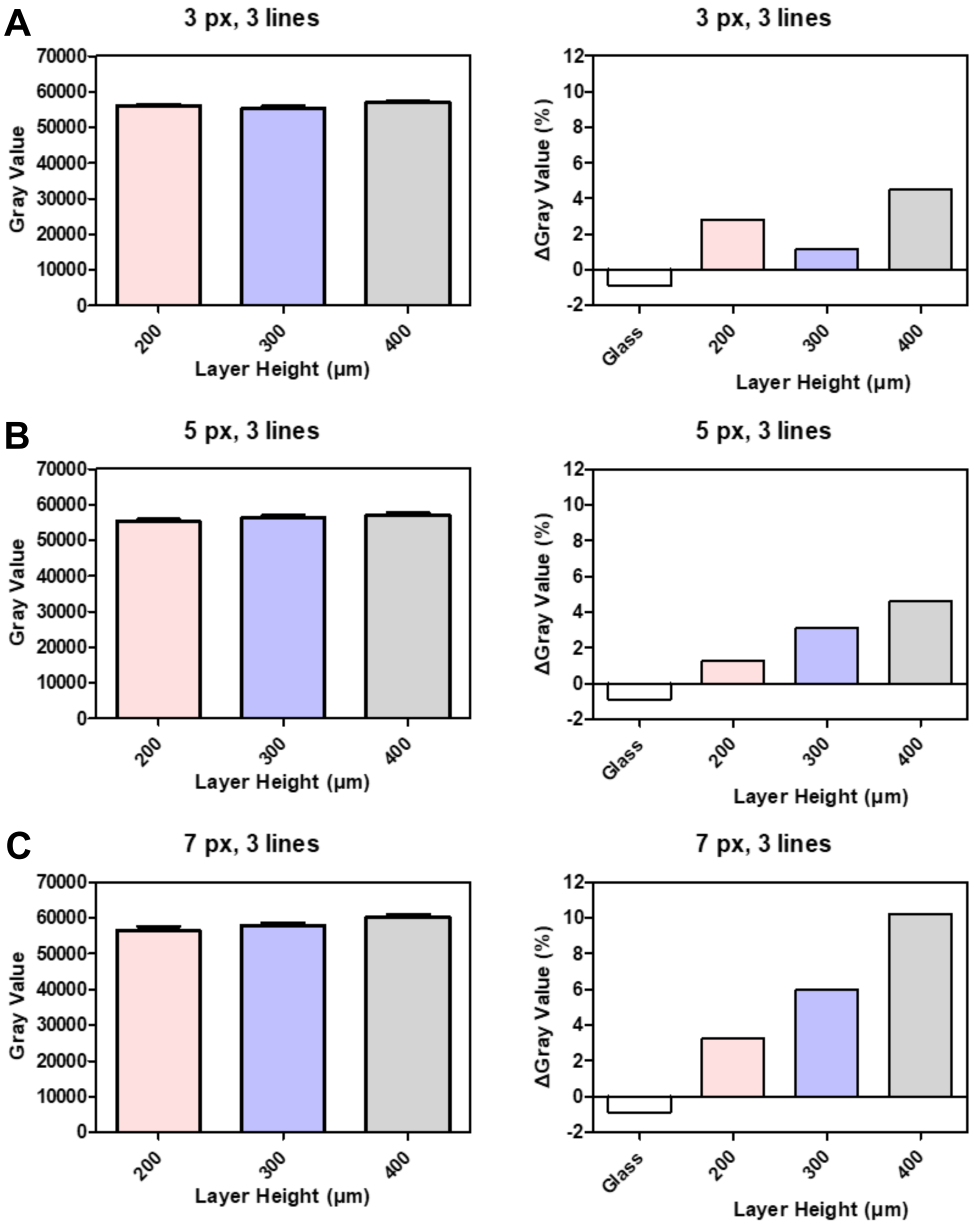

Figure 35. Gray value analysis result and change in gray value (%) for various width of line pattern. The line widths are (A) 3 px, (B) 5 px, and (C) 7 px, respectively.

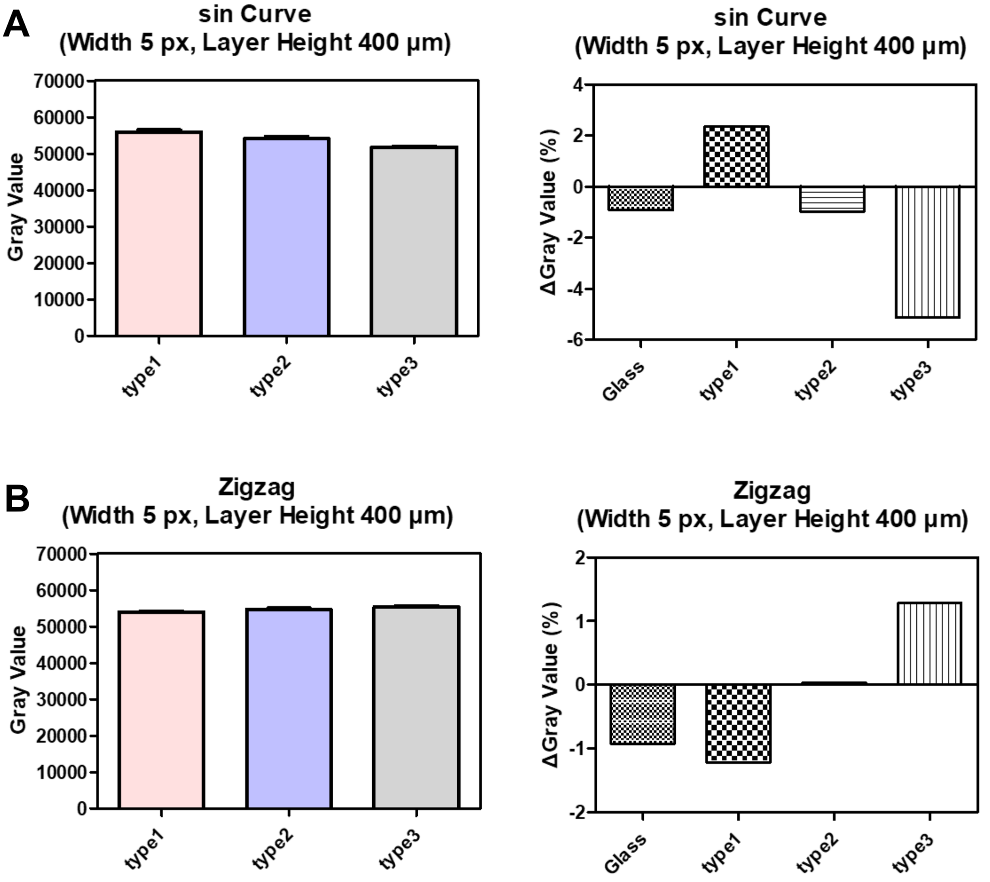

Figure 36. Gray value analysis result and change in gray value (%) for (A) sin curve and (B) zigzag pattern.

3.4.7. Photovoltaic Panel Voltage Analysis of Silk Fibroin Optical Film

Photovoltaic panel voltage analysis was conducted by directly measuring the voltage generated from the photovoltaic panel using a digital multimeter [56]. In the experimental environment, the current of the photovoltaic panel could not be measured, so the generated electrical power was unknown. Therefore, all results are comparison results of changes in the measured PV panel voltage. And, all measurement results were conducted in an arbitrarily set lighting environment, and therefore, it was designed to indirectly examine the results of light diffraction. Measurements were performed under two lighting conditions. First, Figures 37 to 40 are the measurement results when light is applied only on the pattern (Figure 3A). This measurement was investigated to measure only the diffraction effect of light caused by the pattern. The following are the measurement results when the light of Figure 41 is applied to the entire area of the photovoltaic cell (Figure 3B). This measurement was investigated to measure how the effect of the pattern appears in an actual light environment.

PV panel voltage analysis according to the surrounding environment was investigated (Figure 3A and C). In the gray value analysis of the Plain condition, the measured value was worse than that of the Blank condition, but in reality, the voltage was recorded more than twice, indicating the limitation of the gray value analysis (Figure 37). And in the same order as the gray value analysis measured earlier, PV panel voltage analysis according to an area occupied by pattern structure was investigated. Even at 25% of the pattern area, panel voltage still increased (Figure 38A). This is because PV panel voltage can increase even with SF film structure without any pattern structure, such as Plain. Nevertheless, Area-'25%' recorded higher PV panel voltage than the Plain structure. This makes it possible to speculate that high PV panel voltage can be obtained just by the presence of any type of structure. And, in the measurement results according to the number of lines of the pattern structure and the layer height of the hydrogel when the width was fixed at 5

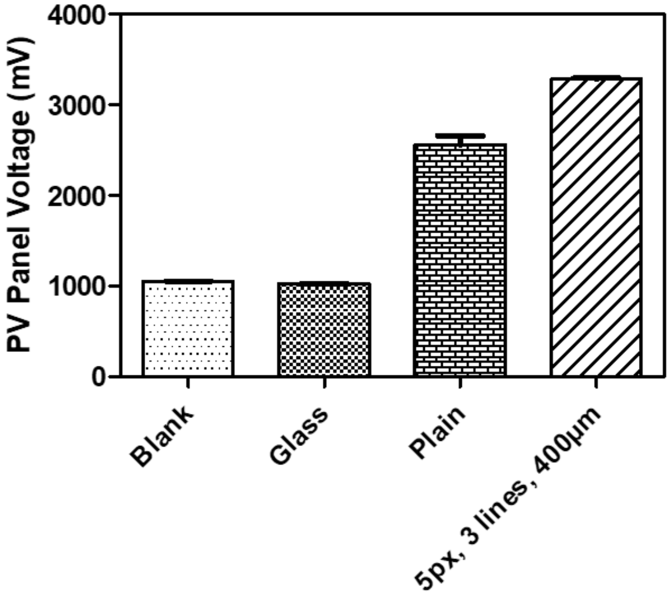

Figure 37. Photovoltaic panel voltage analysis result for comparison of Blank, Glass, Plain, and 5 px, 3 lines, 400 μm conditions.

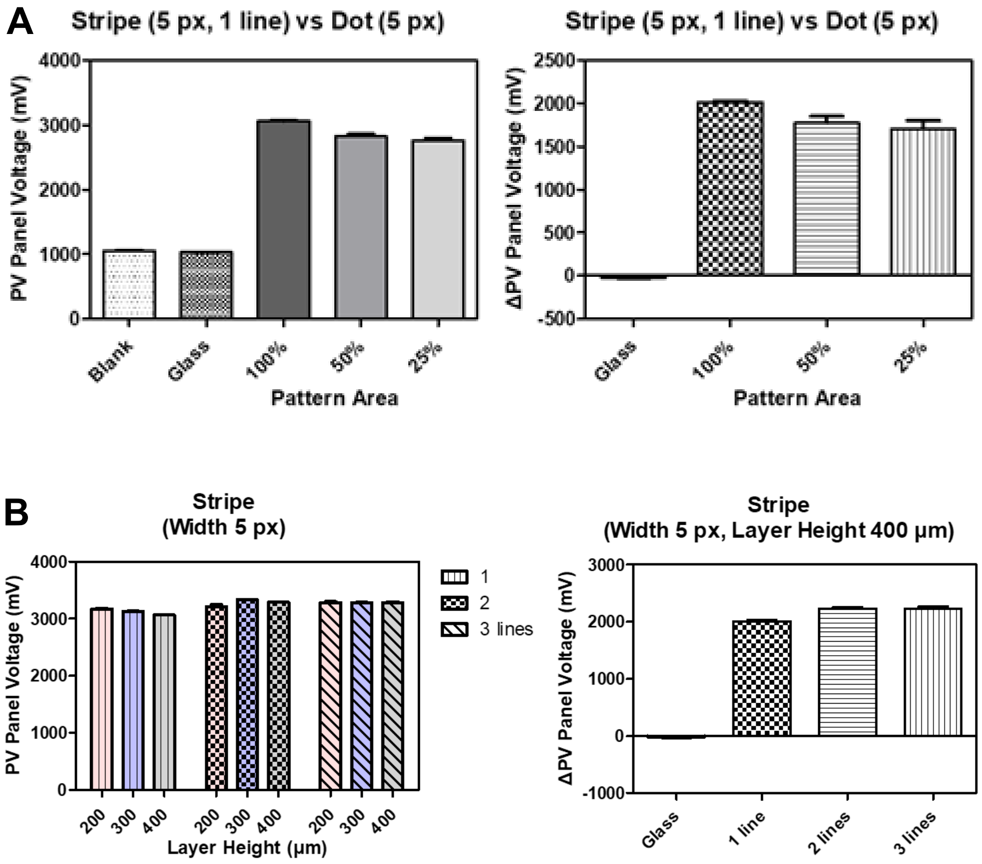

Figure 38. (A) Photovoltaic panel voltage analysis result and change in voltage (%) for various area of pattern. (The stripe is the pattern with 5 px, 1 line, 400 μm, the dot is the pattern with 400 μm) (B) Photovoltaic panel voltage analysis result and change in voltage (%) for various number of line of pattern.

px, the hydrogel layer height condition was not related to the PV panel voltage (Figure 38B). As the number of lines of the pattern increases, the PV panel voltage generally tends to increase. This is because the amount of diffracted light energy increases as the number of lines of the pattern.

As a result of investigating whether the layer height condition of the hydrogel and the width of the line pattern affect the fabrication of the pattern structure (Figure 39), the layer height condition of the hydrogel did not affect the PV panel voltage. Also, the width of the line pattern did not affect the PV panel voltage. The actual measured PV panel voltages did not show a significant difference from the average values. From the gray value analysis results, it was confirmed that the gray value obviously increased (Figure 33-35), but the amount of change in voltage did not show any significant difference. These results imply that more light harvesting is required to change the PV panel voltage. However, a slightly higher standard deviation was measured when the layer height condition of the hydrogel was 200 μm. From this result, it is assumed that a stable structure was not formed under the low layer height condition.

Sin curve structure gives the photovoltaic area where light converges and where it scatters. However, there was no loss in the increment of PV panel voltage. In a sin curve structure, the area occupied by the structure is equal to the Area-'100%' condition. In this condition, the PV panel voltage change was about 2000 mV (Figure 38A), and the PV panel voltage change obtained from the photovoltaic cell due to the sin curve is also about 2000 mV (Figure 40A). However, the standard deviation of the change of PV panel voltage was larger in the sin curve condition (Figure 40A) than in the Area-'100%' condition (Figure 38A). To obtain stable energy conversion efficiency results, the sin curve condition is not a good choice. The zigzag structure also appears where light converges and diverges in the photovoltaic region. However, the change in PV panel voltage was less than 2000 mV (Figure 40B). The zigzag structure may be a worse choice than the sin curve structure.

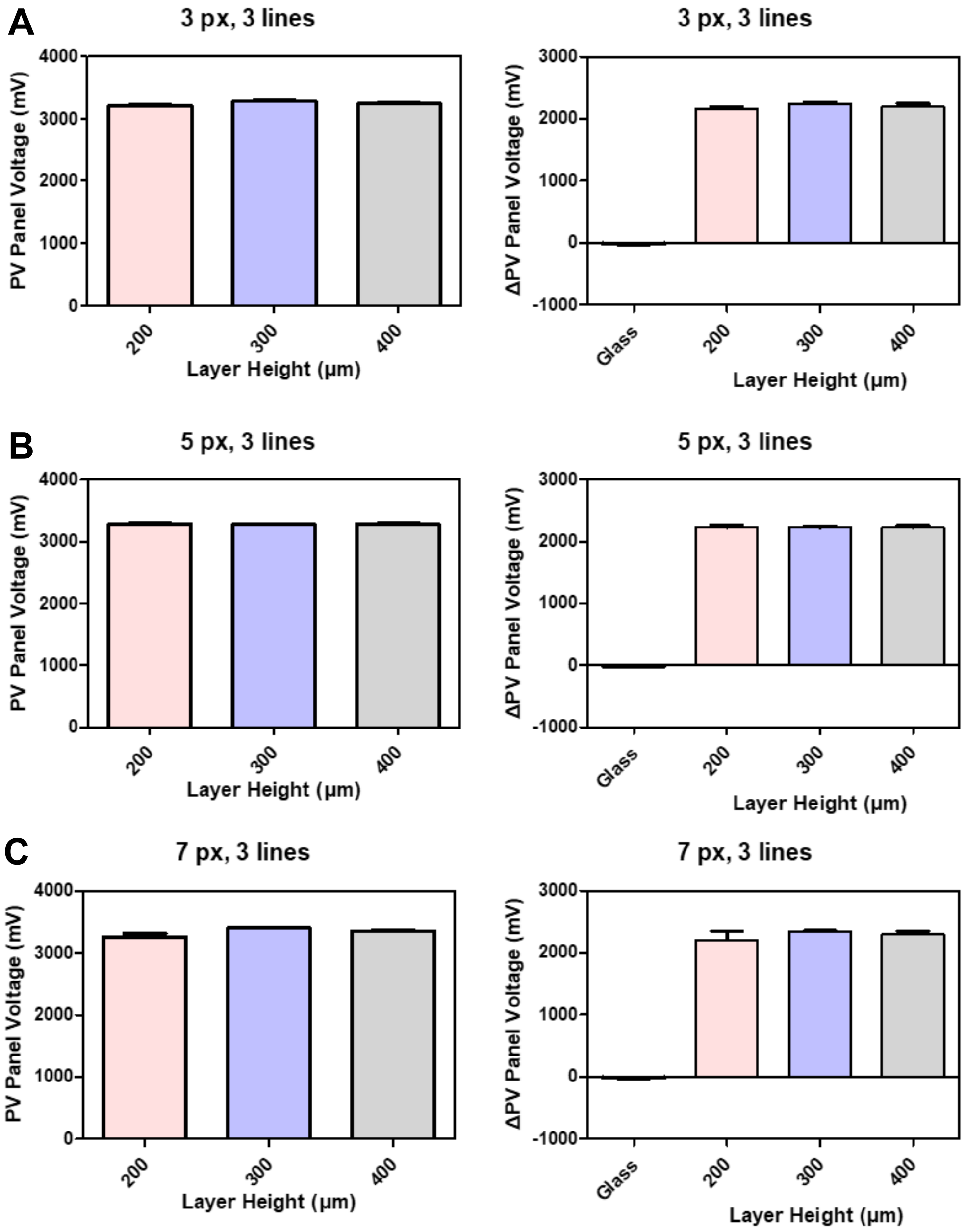

Figure 39. Photovoltaic panel voltage analysis result and change in voltage (%) for various width of line pattern. The line widths are (A) 3 px, (B) 5 px, and (C) 7 px, respectively.

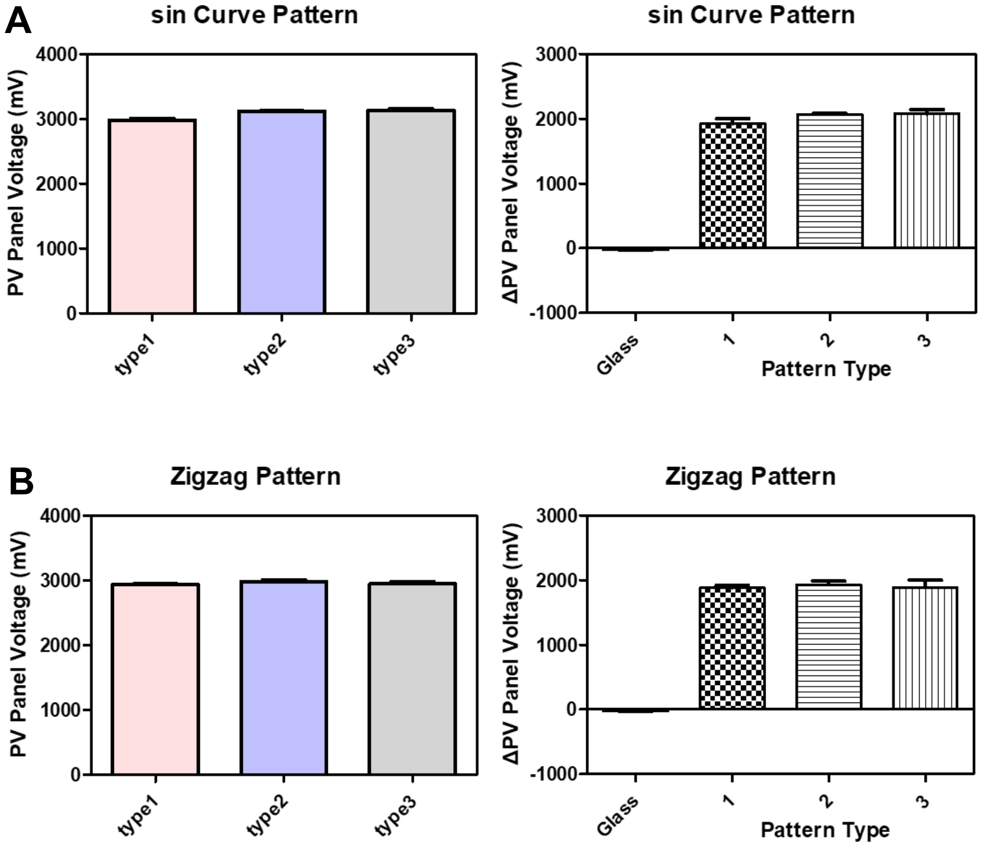

Figure 40. Photovoltaic panel voltage analysis result and change in voltage (%) for (A) sin curve and (B) zigzag pattern.

Finally, the PV panel voltage was measured when the light was applied to the entire photovoltaic cell including the pattern area of the SF optical film (Figure 41). Since the measured voltage varies depending on the brightness of the light source when light is applied to the entire photocell, the measurement was performed while adjusting the brightness by adjusting the gray value of the light source (Figure 10). In the brightness of all light sources, the PV panel voltage was measured lower in the Glass and Plain conditions than in the Blank condition. Since PV panel is generally protected by glass or plastic substrate, the Glass condition can be seen as voltage loss value in the general environment. Therefore, the fact that the Plain condition is similar to or lower than the Glass condition means that the SF film must be patterned under this experimental condition. Plain and 3, 5, and 7 px pattern conditions all showed similar trends, and in all pattern conditions, higher PV panel voltages were measured than in Blank conditions. The illuminance on a clear day is about 100000 lux or more, which corresponds to a gray value of 192. The variation of PV panel voltage was similar from 0 to 192 but generally increased from 192 to 255. Even in the previously measured results, there was a case where the gray value obviously increased (Figure 33-35), but no increase in PV panel voltage was observed (Figure 37-39). This is a result that reconfirms that more light harvesting is needed to increase the voltage of the PV panel. The pattern film generally showed better results than glass in all brightness, suggesting that there is a possibility of applying SF optical film in a power generation environment using actual sunlight.

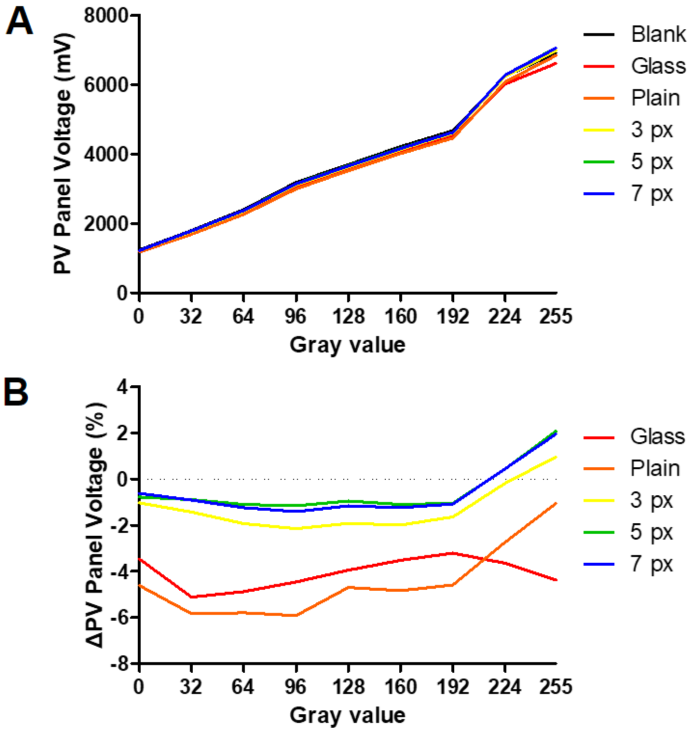

Figure 41. Photovoltaic panel voltage analysis result and change in voltage (%) over the entire photovoltaic cell area. (A) PV panel voltage value according to the brightness of the light source, (B) Change in voltage (%) according to the brightness of the light source. The higher the gray value, the brighter the light source. (All films are 3 lines and 400 μm layer height.)

3.4.8. Limitations of Measurement Method

In general, all samples showed better results than the Blank condition in the gray value analysis. Also, there was no reduction in PV panel voltage analysis than the Plain condition. This means that most of the diffraction patterns presented in the study contribute to the increase in the energy conversion efficiency of photovoltaic cells. However, there were clear differences between patterns. The point to be careful about when interpreting data is that even if a sample has a lower gray value than the Blank condition, the voltage change of the photovoltaic panel does not have a negative value. For example, in the data presented above, the Plain sample showed a lower gray value than the Blank condition, but in PV panel voltage analysis, the Plain sample generates about 2.5 times the voltage of the Blank condition.

There are two reasons for this result. First, the illuminance of the gray value analysis environment is different from the illuminance of the PV panel voltage analysis environment. To proceed with gray value analysis, sample shooting is possible only when a minimum illumination environment is maintained. When the DSLR lens is removed and the surrounding environment is bright, the CCD sensor directly receives surrounding light, resulting in an image that cannot be analyzed. Therefore, when performing gray value analysis, the surroundings should be somewhat dark. On the other hand, when performing PV panel voltage analysis, the brightest light that can be set in the projector passes through a sample. This results in a slightly brighter environment around you. Therefore, it is difficult to directly convert a gray value into PV panel voltage. However, in this study, there was no case where the change in PV panel voltage was negative when the gray value was positive under stripe conditions.

Second, both gray value analysis and PV panel voltage analysis are indirect measurement methods. The purpose of the study is to determine if SF optical film structures diffract light. When the gray value analysis value is higher than the Blank or when the PV panel voltage value is higher than the Blank, it can be qualitatively confirmed that light diffracted, but both methods cannot quantitatively confirm. For example, in the case of sin curve and zigzag patterns, since the vector in the direction where light bends is two-dimensional, it is possible to derive more appropriate results from evaluation through area-type gray value analysis rather than linear-type gray value analysis conducted in this study.

Also, since the current of the PV panel could not be measured, it was not possible to measure how much the power increased compared to the blank condition when diffraction occurred. In general, studies on electrical energy present I-V curves or short-circuit current density [57], or self-calculated efficiencies [56] to discuss improvements. In this study, by examining the increase in gray value and the increase in PV panel voltage, it was found that the diffraction effect of light clearly exists and the electrical energy production increased indirectly. According to previously reported papers, when a diffraction grating was applied to PDMS, the short-circuit current density was improved by about 9.09% [56], and when the nanopatterns was applied to the SF film, the power conversion efficiency was improved by 14.94% [57]. In the organic photovoltaic cell field, which means most polymer solar cells, an improvement of about 13% is considered an excellent result [69], and recently, studies showing an improvement of up to 18% have been reported [75]. The effect of improving the amount of voltage generation was investigated in this study, with voltages ranging from a minimum of 1.62% higher (Figure 41, 192 gray value, 3 px, 3 lines, 400 μm) to a maximum of 6.74% higher (Figure 41, 255 gray value, 5 px, 3 lines, 400 μm) than the condition where glass was placed on the photovoltaic cell under sunlight-like lighting (Figure 41, gray value range in 192-255). However, direct comparison with other research cases is difficult in the current situation where energy conversion efficiency cannot be calculated. Therefore, instead of comparison, this study tried to show that the SF optical film can contribute to light harvesting sufficiently in the sunlight environment through the voltage measurement value (Figure 41) observed when the entire area of the photovoltaic cell is illuminated.

Since SF is a natural polymer material, it is necessary to consider its durability. If SF film is used to increase the amount of electrical energy produced by photovoltaics, the film will be packaged as part of the part and cut off from the external environment. Therefore, aging effects due to UV/Visible light from the sun were considered. In the case of pristine SF, photocrosslinking or photolysis occurs under UV/Visible light [76]. Dityrosine bonds are formed by the photocrosslinking reaction, and the beta-sheet structure is decomposed by the photolysis reaction. According to the study, when aging occurs in the SF structure, the dityrosine bonding increases, and the beta-sheet structure decreases. This phenomenon is positive from the point of view of using DLP printing. However, browning occurs throughout the SF structure, and there is also a possibility that this may adversely affect the energy conversion efficiency [76]. This is a limitation of SF materials.

IV. Conclusion

The SF structures could be printed with an SF ink containing riboflavin as a photoinitiator by DLP 3D printing. The SF solution was clear enough to be printed without formation of beta-sheet structure in the printing process. In the printing system, DLP printing environments were configured by an automated position controller and a DLP printer which were synchronized by separated two computers. Python customized program was created for fabricating SF microneedles and SF optical film structures. Uniquely, the anti-aliasing strategy could enhance the resolution of the SF microstructure by the reduction of step-like features which were a big problem in the DLP printing.

Specifically, SF microneedles were fabricated by DLP 3D printing of SF aqueous solution with riboflavin. Oblique and sharp microneedles were printed using anti-aliasing strategy and shrinkage of hydrogel through dehydration process. The SF microneedles were strong, and no serious damage was observed even under ~300 mN of compressive stress. Besides, SF microneedle arrays were successfully fabricated on the diverse substrates including flexible and hard plastics, metal foil, and glass. The applicability of the SF microneedles was confirmed by delivering fluorescent dye molecules to a model pig skin.

In addition, SF patterns fabricated on a film showed a feasible applicability as an optical film which could harvest the light efficiently by the simple light diffraction. It could collect the light from the hidden areas to the effective solar cells. The light diffraction was investigated by the analysis of gray value and photovoltaic panel voltage. Interestingly, the SF optical film with patterns diffracted light in direction perpendicular to pattern structures and the panel voltage could be increased at least 2.5 times higher compared without SF optical film. Finally, it was confirmed that the photovoltaic cells could produce 1.62–6.74% higher voltage under sunlight-like lighting due to the light diffraction effect of the SF optical film.

SF is a highly recognized protein based material for the biomedical and has been investigated for the wide scope of applications from functional fibers to electronic devices. The reliable printability of the SF inks can enlarge further the potential of a protein based ink in finding new features in the future.

V. References

[1] X. Mu, J.K. Sahoo, P. Cebe, and D.L. Kaplan, Photo-crosslinked silk fibroin for 3D printing, *Polymers*, **2020**, 12, (12), 2936.

[2] N. Kasoju, and U. Bora, Silk fibroin in tissue engineering, *Advanced Healthcare Materials*, **2012**, 1, (4), 393-412.

[3] S. Ghanaati, C. Orth, R.E. Unger, M. Barbeck, M.J. Webber, A. Motta, C. Migliaresi, and C. James Kirkpatrick, Fine-tuning scaffolds for tissue regeneration: effects of formic acid processing on tissue reaction to silk fibroin, *Journal of Tissue Engineering and Regenerative Medicine*, **2010**, 4, (6), 464-472.

[4] D.-H. Kim, J. Viventi, J.J. Amsden, J. Xiao, L. Vigeland, Y.-S. Kim, J.A. Blanco, B. Panilaitis, E.S. Frechette, D. Contreras, D.L. Kaplan, F.G. Omenetto, Y. Huang, K.-C. Hwang, M.R. Zakin, B. Litt, and J.A. Rogers, Dissolvable films of silk fibroin for ultrathin conformal bio-integrated electronics, *Nature Materials*, **2010**, 9, (6), 511-517.

[5] S. Kim, A.N. Mitropoulos, J.D. Spitzberg, H. Tao, D.L. Kaplan, and F.G. Omenetto, Silk inverse opals, *Nature Photonics*, **2012**, 6, (12), 818-823.

[6] L.-D. Koh, Y. Cheng, C.-P. Teng, Y.-W. Khin, X.-J. Loh, S.-Y. Tee, M. Low, E. Ye, H.-D. Yu, Y.-W. Zhang, and M.-Y. Han, Structures, mechanical properties and applications of silk fibroin materials, *Progress in Polymer Science*, **2015**, 46, 86-110.

[7] B. Zhu, H. Wang, W.R. Leow, Y. Cai, X.J. Loh, M.-Y. Han, and X. Chen, Silk fibroin for flexible electronic devices, *Advanced Materials*, **2016**, 28, (22), 4250-4265.

[8] M.B. Applegate, B.P. Partlow, J. Coburn, B. Marelli, C. Pirie, R. Pineda, D.L. Kaplan, and F.G. Omenetto, Photocrosslinking of silk fibroin using riboflavin for ocular prostheses, *Advanced Materials*, **2016**, 28, (12), 2417-2420.

[9] J.P. Mondia, J.J. Amsden, D. Lin, L.D. Negro, D.L. Kaplan, and F.G. Omenetto, Rapid nanoimprinting of doped silk films for enhanced fluorescent emission, *Advanced Materials*, **2010**, 22, (41), 4596-4599.

[10] X. Cui, B.G. Soliman, C.R. Alcala-Orozco, J. Li, M.A. Vis, M. Santos, S.G. Wise, R. Levato, J. Malda, and T.B. Woodfield, Rapid photocrosslinking of silk hydrogels with high cell density and enhanced shape fidelity, *Advanced Healthcare Materials*, **2020**, 9, (4), 1901667.

[11] S.H. Kim, Y.K. Yeon, J.M. Lee, J.R. Chao, Y.J. Lee, Y.B. Seo, M. Sultan, O.J. Lee, J.S. Lee, and S.-i. Yoon, Precisely printable and biocompatible silk fibroin bioink for digital light processing 3D printing, *Nature Communications*, **2018**, 9, (1), 1-14.

[12] T.D. Ngo, A. Kashani, G. Imbalzano, K.T. Nguyen, and D. Hui, Additive manufacturing (3D printing): A review of materials, methods, applications and challenges, *Composites Part B: Engineering*, **2018**, 143, 172-196.

[13] C.W. Hull, The birth of 3D printing, *Research-Technology Management*, **2015**, 58, (6), 25-30.

[14] C. Liao, A. Wuethrich, and M. Trau, A material odyssey for 3D nano/microstructures: two photon polymerization based nanolithography in bioapplications, *Applied Materials Today*, **2020**, 19, 100635.

[15] F.P. Melchels, J. Feijen, and D.W. Grijpma, A review on stereolithography and its applications in biomedical engineering, *Biomaterials*, **2010**, 31, (24), 6121-6130.

[16] S. Vock, B. Klöden, A. Kirchner, T. Weißgärber, and B. Kieback, Powders for powder bed fusion: a review, *Progress in Additive Manufacturing*, **2019**, 4, (4), 383-397.

[17] O.A. Mohamed, S.H. Masood, and J.L. Bhowmik, Optimization of fused deposition modeling process parameters: a review of current research and future prospects, *Advances in Manufacturing*, **2015**, 3, (1), 42-53.

[18] S.F.S. Shirazi, S. Gharehkhani, M. Mehrali, H. Yarmand, H.S.C. Metselaar, N.A. Kadri, and N.A.A. Osman, A review on powder-based additive manufacturing for tissue engineering: selective laser sintering and inkjet 3D printing, *Science and Technology of Advanced Materials*, **2015**, 16, (3), 033502.

[19] M. Vaezi, H. Seitz, and S. Yang, A review on 3D micro-additive manufacturing technologies, *The International Journal of Advanced Manufacturing Technology*, **2013**, 67, (5), 1721-1754.

[20] X. Wang, M. Jiang, Z. Zhou, J. Gou, and D. Hui, 3D printing of polymer matrix composites: A review and prospective, *Composites Part B: Engineering*, **2017**, 110, 442-458.

[21] M.M. Prabhakar, A. Saravanan, A.H. Lenin, K. Mayandi, and P.S. Ramalingam, A short review on 3D printing methods, process parameters and materials, *Materials Today: Proceedings*, **2021**, 45, 6108-6114.

[22] I. Cooperstein, M. Layani, and S. Magdassi, 3D printing of porous structures by UV-curable O/W emulsion for fabrication of conductive objects, *Journal of Materials Chemistry C*, **2015**, 3, (9), 2040-2044.

[23] D. Shin, and J. Hyun, Silk fibroin microneedles fabricated by digital light processing 3D printing, *Journal of Industrial and Engineering Chemistry*, **2021**, 95, 126-133.

[24] H. Lee, D. Shin, S. Shin, and J. Hyun, Effect of gelatin on dimensional stability of silk fibroin hydrogel structures fabricated by digital light processing 3D printing, *Journal of Industrial and Engineering Chemistry*, **2020**, 89, 119-127.

[25] E.M. Maines, M.K. Porwal, C.J. Ellison, and T.M. Reineke, Sustainable advances in SLA/DLP 3D printing materials and processes, *Green Chemistry*, **2021**, 23, (18), 6863-6897.

[26] Z. Zhao, X. Tian, and X. Song, Engineering materials with light: recent progress in digital light processing based 3D printing, *Journal of Materials Chemistry C*, **2020**, 8, (40), 13896-13917.

[27] X. Peng, L. Yue, S. Liang, S. Montgomery, C. Lu, C.-M. Cheng, R. Beyah, R.R. Zhao, and H.J. Qi, Multi-Color 3D Printing via Single-Vat Grayscale Digital Light Processing, *Advanced Functional Materials*, **2022**, 32, (28), 2112329.

[28] C. Zhou, and Y. Chen, Additive manufacturing based on optimized mask video projection for improved accuracy and resolution, *Journal of Manufacturing Processes*, **2012**, 14, (2), 107-118.

[29] A. Andreu, P.-C. Su, J.-H. Kim, C.S. Ng, S. Kim, I. Kim, J. Lee, J. Noh, A.S. Subramanian, and Y.-J. Yoon, 4D printing materials for vat photopolymerization, *Additive Manufacturing*, **2021**, 44, 102024.

[30] R. Langer, Transdermal drug delivery: past progress, current status, and future prospects, *Advanced drug delivery reviews*, **2004**, 56, (5), 557-558.

[31] S. Sharma, K. Hatware, P. Bhadane, S. Sindhikar, and D.K. Mishra, Recent advances in microneedle composites for biomedical applications: Advanced drug delivery technologies, *Materials Science and Engineering: C*, **2019**, 103, 109717.

[32] J.L. Liu, Y.H. Feng, X.P. Zhang, D.D. Zhu, L.Q. Zhang, and X.D. Guo, Experimental and theoretical studies of drug-polymer interactions to control the drug distributions in dissolving microneedles, *Journal of Industrial and Engineering Chemistry*, **2020**, 84, 280-289.

[33] L.Q. Zhang, X.P. Zhang, Y.Y. Hao, B.L. Zhang, and X.D. Guo, Codelivery of hydrophilic and hydrophobic drugs in a microneedle patch for the treatment of skin pigmentation, *Journal of Industrial and Engineering Chemistry*, **2020**, 88, 241-250.

[34] S. Chandrasekaran, J.D. Brazzle, and A.B. Frazier, Surface micromachined metallic microneedles, *Journal of Microelectromechanical Systems*, **2003**, 12, (3), 281-288.

[35] H.J. Gardeniers, R. Luttge, E.J. Berenschot, M.J. De Boer, S.Y. Yeshurun, M. Hefetz, R. Van't Oever, and A. Van Den Berg, Silicon micromachined hollow microneedles for transdermal liquid transport, *Journal of Microelectromechanical Systems*, **2003**, 12, (6), 855-862.

[36] N. Wilke, A. Mulcahy, S.-R. Ye, and A. Morrissey, Process optimization and characterization of silicon microneedles fabricated by wet etch technology, *Microelectronics Journal*, **2005**, 36, (7), 650-656.

[37] J.-H. Park, M.G. Allen, and M.R. Prausnitz, Biodegradable polymer microneedles: fabrication, mechanics and transdermal drug delivery, *Journal of Controlled Release*, **2005**, 104, (1), 51-66.

[38] H. Takahashi, Y. Jung Heo, N. Arakawa, T. Kan, K. Matsumoto, R. Kawano, and I. Shimoyama, Scalable fabrication of microneedle arrays via spatially controlled UV exposure, *Microsystems & Nanoengineering*, **2016**, 2, (1), 1-9.

[39] Y. Lu, S.N. Mantha, D.C. Crowder, S. Chinchilla, K.N. Shah, Y.H. Yun, R.B. Wicker, and J.-W. Choi, Microstereolithography and characterization of poly (propylene fumarate)-based drug-loaded microneedle arrays, *Biofabrication*, **2015**, 7, (4), 045001.

[40] A.R. Johnson, C.L. Caudill, J.R. Tumbleston, C.J. Bloomquist, K.A. Moga, A. Ermoshkin, D. Shirvanyants, S.J. Mecham, J.C. Luft, and J.M. DeSimone, Single-step fabrication of computationally designed microneedles by continuous liquid interface production, *PloS One*, **2016**, 11, (9), e0162518.

[41] S.H. Lim, J.Y. Ng, and L. Kang, Three-dimensional printing of a microneedle array on personalized curved surfaces for dual-pronged treatment of trigger finger, *Biofabrication*, **2017**, 9, (1), 015010.

[42] A.R. Johnson, and A.T. Procopio, Low cost additive manufacturing of microneedle masters, *3D printing in Medicine*, **2019**, 5, (1), 1-10.

[43] H. Lin, D. Zhang, P.G. Alexander, G. Yang, J. Tan, A.W.-M. Cheng, and R.S. Tuan, Application of visible light-based projection stereolithography for live cell-scaffold fabrication with designed architecture, *Biomaterials*, **2013**, 34, (2), 331-339.

[44] C. Sun, N. Fang, D. Wu, and X. Zhang, Projection micro-stereolithography using digital micro-mirror dynamic mask, *Sensors and Actuators A: Physical*, **2005**, 121, (1), 113-120.

[45] I.-B. Park, Y.-M. Ha, and S.-H. Lee, Still motion process for improving the accuracy of latticed microstructures in projection microstereolithography, *Sensors and Actuators A: Physical*, **2011**, 167, (1), 117-129.

[46] K. Lee, and H. Jung, Drawing lithography for microneedles: A review of fundamentals and biomedical applications, *Biomaterials*, **2012**, 33, (30), 7309-7326.

[47] Z. Chen, R. Ye, J. Yang, Y. Lin, W. Lee, J. Li, L. Ren, B. Liu, and L. Jiang, Rapidly fabricated microneedle arrays using magnetorheological drawing lithography for transdermal drug delivery, *ACS Biomaterials Science & Engineering*, **2019**, 5, (10), 5506-5513.

[48] S. Pradeep Narayanan, and S. Raghavan, Solid silicon microneedles for drug delivery applications, *The International Journal of Advanced Manufacturing Technology*, **2017**, 93, (1), 407-422.

[49] J. Li, B. Liu, Y. Zhou, Z. Chen, L. Jiang, W. Yuan, and L. Liang, Fabrication of a Ti porous microneedle array by metal injection molding for transdermal drug delivery, *PloS One*, **2017**, 12, (2), e0172043.

[50] K.A. Moga, L.R. Bickford, R.D. Geil, S.S. Dunn, A.A. Pandya, Y. Wang, J.H. Fain, C.F. Archuleta, A.T. O'Neill, and J.M. DeSimone, Rapidly–dissolvable microneedle patches via a highly scalable and reproducible soft lithography approach, *Advanced Materials*, **2013**, 25, (36), 5060-5066.

[51] T. Yucel, M.L. Lovett, and D.L. Kaplan, Silk-based biomaterials for sustained drug delivery, *Journal of Controlled Release*, **2014**, 190, 381-397.

[52] X. You, J.-h. Chang, B.-K. Ju, and J.J. Pak, Rapidly dissolving fibroin microneedles for transdermal drug delivery, *Materials Science and Engineering: C*, **2011**, 31, (8), 1632-1636.

[53] J.A. Stinson, W.K. Raja, S. Lee, H.B. Kim, I. Diwan, S. Tutunjian, B. Panilaitis, F.G. Omenetto, S. Tzipori, and D.L. Kaplan, Silk fibroin microneedles for transdermal vaccine delivery, *ACS Biomaterials Science & Engineering*, **2017**, 3, (3), 360-369.

[54] S. Deng, J. Wu, M.D. Dickey, Q. Zhao, and T. Xie, Rapid open-air digital light 3D printing of thermoplastic polymer, *Advanced Materials*, **2019**, 31, (39), 1903970.

[55] R.D. Boehm, P.R. Miller, R. Singh, A. Shah, S. Stafslien, J. Daniels, and R.J. Narayan, Indirect rapid prototyping of antibacterial acid anhydride copolymer microneedles, *Biofabrication*, **2012**, 4, (1), 011002.

[56] Y.J. Kim, Y.J. Yoo, D.E. Yoo, D.W. Lee, M.S. Kim, H.J. Jang, Y.-C. Kim, J.-H. Jang, I.S. Kang, and Y.M. Song, Enhanced light harvesting in photovoltaic devices using an edge-located one-dimensional grating polydimethylsiloxane membrane, *ACS Applied Materials & Interfaces*, **2019**, 11, (39), 36020-36026.

[57] C. Malinowski, F. He, Y. Zhao, I. Chang, D.W. Hatchett, S. Zhai, and H. Zhao, Nanopatterned silk fibroin films with high transparency and high haze for optical applications, *RSC Advances*, **2019**, 9, (70), 40792-40799.

[58] M.K. DeBari, C.I. King, III, T.A. Altgold, and R.D. Abbott, Silk fibroin as a green material, *ACS Biomaterials Science & Engineering*, **2021**, 7, (8), 3530-3544.

[59] D.N. Rockwood, R.C. Preda, T. Yücel, X. Wang, M.L. Lovett, and D.L. Kaplan, Materials fabrication from Bombyx mori silk fibroin, *Nature Protocols*, **2011**, 6, (10), 1612-1631.

[60] S.Y. Yang, E.D. O'Cearbhaill, G.C. Sisk, K.M. Park, W.K. Cho, M. Villiger, B.E. Bouma, B. Pomahac, and J.M. Karp, A bio-inspired swellable microneedle adhesive for mechanical interlocking with tissue, *Nature Communications*, **2013**, 4, (1), 1-10.

[61] W. Chen, R. Tian, C. Xu, B.C. Yung, G. Wang, Y. Liu, Q. Ni, F. Zhang, Z. Zhou, and J. Wang, Microneedle-array patches loaded with dual mineralized protein/peptide particles for type 2 diabetes therapy, *Nature Communications*, **2017**, 8, (1), 1-11.

[62] R. Li, L. Zhang, X. Jiang, L. Li, S. Wu, X. Yuan, H. Cheng, X. Jiang, and M. Gou, 3D-printed microneedle arrays for drug delivery, *Journal of Controlled Release*, **2022**, 350, 933-948.

[63] M. Ochoa, J. Zhou, R. Rahimi, V. Badwaik, D. Thompson, and B. Ziaie, Rapid 3D-print-and-shrink fabrication of biodegradable microneedles with complex geometries, *IEEE 2015 Transducers - 2015 18th International Conference on Solid-State Sensors, Actuators and Microsystems (TRANSDUCERS), Anchorage, AK, USA*, **2015**, 1251-1254.

[64] D. Oran, S.G. Rodriques, R. Gao, S. Asano, M.A. Skylar-Scott, F. Chen, P.W. Tillberg, A.H. Marblestone, and E.S. Boyden, 3D nanofabrication by volumetric deposition and controlled shrinkage of patterned scaffolds, *Science*, **2018**, 362, (6420), 1281-1285.

[65] M.R. Prausnitz, and R. Langer, Transdermal drug delivery, *Nature Biotechnology*, **2008**, 26, (11), 1261-1268.

[66] M.J. Kim, S.C. Park, B. Rizal, G. Guanes, S.-K. Baek, J.-H. Park, A.R. Betz, and S.-O. Choi, Fabrication of circular obelisk-type multilayer microneedles using micro-milling and spray deposition, *Frontiers in Bioengineering and Biotechnology*, **2018**, 6, 54.

[67] N. Elahpour, F. Pahlevanzadeh, M. Kharaziha, H.R. Bakhsheshi-Rad, S. Ramakrishna, and F. Berto, 3D printed microneedles for transdermal drug delivery: A brief review of two decades, *International Journal of Pharmaceutics*, **2021**, 597, 120301.

[68] R. Wang, G. Jiang, U.E. Aharodnikau, K. Yunusov, Y. Sun, T. Liu, and S.O. Solomevich, Recent advances in polymer microneedles for drug transdermal delivery: Design strategies and applications, *Macromolecular Rapid Communications*, **2022**, 43, (8), 2200037.

[69] G.J. Hedley, A. Ruseckas, and I.D.W. Samuel, Light harvesting for organic photovoltaics, *Chemical Reviews*, **2017**, 117, (2), 796-837.

[70] G.D. Scholes, G.R. Fleming, A. Olaya-Castro, and R. Van Grondelle, Lessons from nature about solar light harvesting, *Nature Chemistry*, **2011**, 3, (10), 763-774.

[71] H. Tao, D.L. Kaplan, and F.G. Omenetto, Silk materials–a road to sustainable high technology, *Advanced Materials*, **2012**, 24, (21), 2824-2837.

[72] N. Kato, S. Ikeda, M. Hirakawa, K. Nishimori, and H. Ito, Relationship between degree of polymerization and optical and thermal properties of Bisphenol-A in polycarbonate polymers, *AIP Conference Proceedings*, **2019**, 2065, 030018.

[73] N. Kato, S. Ikeda, M. Hirakawa, and H. Ito, Correlation of the abbe number, the refractive index, and glass transition temperature to the degree of polymerization of norbornane in polycarbonate polymers, *Polymers*, **2020**, 12, (11), 2484.

[74] N. Kato, S. Ikeda, M. Hirakawa, and H. Ito, Relationship between degree of polymerization and optical and thermal properties of fluorene in polycarbonate polymers, *Journal of Applied Polymer Science*, **2017**, 134, (30), 45042.

[75] M.S.A. Kamel, A. Al-jumaili, M. Oelgemöller, and M.V. Jacob, Inorganic nanoparticles to overcome efficiency inhibitors of organic photovoltaics: An in-depth review, *Renewable and Sustainable Energy Reviews*, **2022**, 166, 112661.

[76] S. Lee, S.H. Kim, Y.-Y. Jo, W.-T. Ju, H.-B. Kim, and H. Kweon, Effects of ultraviolet light irradiation on silk fibroin films prepared under different conditions, *Biomolecules*, **2021**, 11, (1), 70.

VI. Appendix

DLP Printing Systems

```
;Ctrl+S Start, Ctrl+T End

^s::
zposition:=38000 ;Start point
refresh:=zposition-5000 ;Refresh variable
c_base:=0
c_needle:=0

Base: ;Fabrication of base film
envadd,c_base,1

Click 85,180 ;Position controller program
send,{backspace 6}
StringTrimLeft,msg,zposition,0
send,%msg%
send,{enter}
envadd,zposition,-50
sleep, 145000

Click 85,180
send,{backspace 6}
StringTrimLeft,msg,refresh,0
send,%msg%
send,{enter}
envadd,refresh,-50
sleep, 5000

if c_base<3
goto Base

Needle: ;Fabrication of microneedles
envadd,c_needle,1

Click 85,180
send,{backspace 6}
StringTrimLeft,msg,zposition,0
send,%msg%
send,{enter}
envadd,zposition,-50
sleep, 145000

Click 85,180
send,{backspace 6}
```

```
StringTrimLeft,msg,refresh,0
send,%msg%
send,{enter}
envadd,refresh,-10
sleep, 5000

if c_needle<100
goto Needle

msgbox, DONE

^t::exitapp
return

```

Microneedles

```
from PIL import Image

"""initialization"""
row = 15
col = 15
base = 6
distance = 15
needle_height = 1000
layer_height = 50
"""##############"""

width = col * base + (col - 1) * distance + 70
height = row * base + (row - 1) * distance + 70

file_number = 0
for i in range(0, 5):
    im = Image.new("L", (width, height), 255)
    file_name = str(file_number).zfill(4) + '.bmp'
    file_number = file_number + 1
    im.save(file_name)

layer = (int)(needle_height / layer_height)
BASE = base
if BASE % 2 == 1:
    BASE = BASE + 1
BASE = (int)(BASE / 2) - 1
node = [0]
for i in range(1, BASE):
    node.append(i * (int)(layer/BASE))
node.append(layer)
print(node)

alpha = 0
for I in range(1, BASE + 1):
    K = 0
    for J in range(node[I-1], node[I]):
        im = Image.new("L", (width, height), 0)
        im_raw = im.load()

        """y=-3.140 + 61.28x + 49.13x^2"""
        GRAY = (int)(255 / (node[I] - node[I-1]))
        for i in range(0, row):
            for j in range(0, col):
                x = 30 + i * (base + distance)
                y = 30 + j * (base + distance)
                for X in range(x + alpha, x + base - alpha):
                    for Y in range(y + alpha, y + base - alpha):
```

```
                        TEMP = (int)(256 * (pow(100 * (255 -
                                GRAY * K) / 256 / 49 +
                                0.45, 0.5) - 0.62))
                        im_raw[Y, X] = TEMP
        K = K + 1
        for i in range(0, row):
            for j in range(0, col):
                x = 30 + i * (base + distance)
                y = 30 + j * (base + distance)
                if alpha + 1 < base - alpha - 1:
                    for X in range(x + alpha + 1, x + base -
                                   alpha - 1):
                         for Y in range(y + alpha + 1, y +
                                        base - alpha - 1):
                            im_raw[Y, X] = 255

        file_name = str(file_number).zfill(4) + '.bmp'
        file_number = file_number + 1
        im.save(file_name)
    alpha = alpha + 1

for i in range(0, 5):
    im = Image.new("L", (width, height), 0)
    file_name = str(file_number).zfill(4) + '.bmp'
    file_number = file_number + 1
    im.save(file_name)
```

Sin function curve

```
import math
from PIL import Image

PI = math.pi
"""
RAD_DEG360 = math.radians(360)
DEG_RAD2PI = math.degrees(2*PI)
print(PI)
print(RAD_DEG360)
print(DEG_RAD2PI)
"""

img_px_width = 256
img_px_height = 11
curve_img = Image.new("RGB", (img_px_width, img_px_height))
times = 4
for x in range(0, img_px_width):
    x_rad = math.radians(x*360*times/img_px_width)
    sin_result = math.sin(x_rad)
    sin_result = 3 * sin_result
    round_sin_result = round(sin_result)
    y = round_sin_result
    y = -y
    curve_img.putpixel((x, y + 3), (255, 255, 255))
    curve_img.putpixel((x, y + 4), (255, 255, 255))
    curve_img.putpixel((x, y + 5), (255, 255, 255))
    curve_img.putpixel((x, y + 6), (255, 255, 255))
    curve_img.putpixel((x, y + 7), (255, 255, 255))

curve_img.save("sin_curve_pattern.bmp")

```

Zigzag curve

```python
import math
from PIL import Image

img_px_width = 292
img_px_height = 11
curve_img = Image.new("RGB", (img_px_width, img_px_height))
times = 4
line_pattern_width = round((img_px_width / 2) / times)
A = (img_px_height - 4 - 1) / line_pattern_width

for time in range(0, times):
    x_position = time * 2 * line_pattern_width
    for X in range(0, line_pattern_width):
        y = round(A * X)
        x = X + x_position
        curve_img.putpixel((x, y), (255, 255, 255))
        curve_img.putpixel((x, y + 1), (255, 255, 255))
        curve_img.putpixel((x, y + 2), (255, 255, 255))
        curve_img.putpixel((x, y + 3), (255, 255, 255))
        curve_img.putpixel((x, y + 4), (255, 255, 255))
    x_position = x_position + line_pattern_width
    for X in range(0, line_pattern_width):
        y = round((-1 * A) * X + (img_px_height - 4 - 1))
        x = X + x_position
        if x == img_px_width:
            break
        curve_img.putpixel((x, y), (255, 255, 255))
        curve_img.putpixel((x, y + 1), (255, 255, 255))
        curve_img.putpixel((x, y + 2), (255, 255, 255))
        curve_img.putpixel((x, y + 3), (255, 255, 255))
        curve_img.putpixel((x, y + 4), (255, 255, 255))

curve_img.save("zigzag_pattern.bmp")
```

초 록

SF (Silk fibroin)는 생체적합성이 높아 현재 다양한 분야에서 사용되는 천연 단백질 재료다. 최근에 리보플라빈을 이용한 SF 분자의 광가교 반응 기작이 보고된 이후로, 디지털 광원 처리 (Digital Light Processing, DLP) 기술을 사용한 SF의 3D 프린팅 연구가 활발히 진행되고 있다. 광개시제로서 리보플라빈은 350-450 nm 영역의 빛을 흡수하여 라디칼을 형성하고, 이 때 SF는 광산화를 통해 디티로신 결합을 형성하여 하이드로겔 네트워크를 만든다. SF의 광가교 반응에 리보플라빈을 사용하는 것은 상당히 도전적이며 기존에 연구된 사례 또한 드물다. 그러나 SF와 리보플라빈만으로 생체적합성이 높으며 형태를 잘 유지하는 3D 프린팅 구조체를 제작할 수 있어 연구의 가치가 있다. SF의 광가교 반응을 활용하기 위함뿐만 아니라, DLP 프린팅에 안티 앨리어싱 전략을 도입하면 계단 현상을 줄여 SF 패턴의 분해능을 높일 수 있다. 분해능은 DLP 프린팅에 사용되는 장비의 하드웨어적 한계인데, 분해능의 개선을 위해서는 그레이스케일 처리, 픽셀 단위의 이미지 조정 등의 이미지 처리 과정을 거쳐야 한다. 본 연구에서는 그레이스케일 처리를 통한 소프트웨어적 개선으로 DLP 프로젝터 분해능의 하드웨어적 한계를 극복했다. 이렇게 SF 3D 프린팅 구조체의 향상된 분해능은 마이크로니들의 더 작고 날카로운 구조를 통해 평가된다. 본 연구에서는 SF 마이크로니들을 제작하고 돼지 피부에 대한 관통 시험을 통해 마이크로니들의 성능을 평가했다. 또한 픽셀 단위 이미지 조정을 통해 DLP 프린팅을 위한 3D 모델 생성 과정을 생략할 수 있다. DLP 패턴 이미지는 2차원 비트맵이므로 이미지를 픽셀 단위로 조정하여 원하는 모양의 구조를 인쇄할 수 있으며, 이는 비교적 큰 크기의 구조물을 생성하여 확인된다. 본 연구에서는 빛 수확을 위한 광학 필름 구조를 제작하고 주요 회절 특성을 조사하였다. 제작한 SF

광학 필름 구조체를 이용해 광전지에서 최소 1.62%, 최대 6.74% 더 많은 전압이 생산되는 것을 확인했다. 본 연구 자료는 SF의 DLP 프린팅 응용을 위한 탐구 결과를 제시함으로써 단백질 기반 잉크의 활용 분야를 더 넓히는 계기가 될 것이다.

색인어: 실크 피브로인, 3D 프린팅, 디지털 광원 처리, 안티 앨리어싱, 마이크로니들, 광학 필름.

학 번: 2016-21475

감사의 글

제가 드디어 박사과정을 마치고 관악을 떠납니다. 학부 입학부터 지금까지 정말 오랜 시간이 지났습니다. 아주 어린 시절 시작된 제 삶의 첫번째 막이 컴퓨터과학에 대한 몰입과 집중이었다면, 청년 시절 인생의 두번째 막은 바이오소재공학에 대한 호기심과 도전이었습니다. 이번 막은 지금까지 겪은 모든 삶의 파도에서 가장 높은 마루와 가장 깊은 골에 부딪혔던 격랑의 연속이었습니다. 혼자 감당하기 어려운 순간들에 수많은 사람들의 도움이 있었고 그 덕분에 지금의 제가 존재하고 있습니다. 감사합니다. 이제 세번째 막을 준비하기 위한 막간의 시간을 맞이하니, 소중한 추억들과 고마운 사람들이 떠오릅니다.

박사과정 동안 탐구했던 연구들을 정리하고 이 논문을 완성하기까지 저의 지도교수이신 현진호 교수님의 셀 수 없는 가르침과 조언이 있었습니다. 정말 감사드립니다. 또한 심사 과정에서 제 부족한 글이 더 나아질 수 있게 진정으로 도와주신 이기훈 교수님, 김태일 교수님, 기창석 교수님, 곽선영 교수님께 감사드립니다. 그리고 심사를 위해 먼 걸음 해주신 윤규식 교수님께도 깊은 감사를 드립니다. 교수님들께서 제게 주신 소중한 말씀들 덕분에 학위과정을 마칠 수 있었습니다.

처음 대학원 생활을 시작했을 때부터 지금까지 많은 도움을 주신 선배님들께 감사드립니다. 박민성 박사님, 신성철 교수님, 그리고 이소라 박사님의 조언들은 탐구하는 방법과 생각의 방향을 찾는 데 큰 힘이 되었습니다. 그리고 학부 시절부터 언제나 제 편에 서서 같이 인생에 대해 고민해주는, 의지할 수 있는 친구들 백지선, 김가영, 김다현, 정성아, 이현지에게 감사드립니다. 여러분과 이렇게 오랜 시간 함께할 수 있어서 행복합니다. 또한 가장 힘든 시기를 보내고 있을 때 마음의 위로가 되어준 이동한, 이시영에게 감사드립니다. 덕분에 버텨낼 수 있었고 지금 이 순간을 맞이했습니다. 어릴 적부터 오랜 바램이었던

요트 세일링을 Deepika Thakur, 이희현과 함께 즐겼던 시간 또한 잊지 못할 것입니다. 특별한 경험을 공유하게 되어 영광입니다. 그리고 기나긴 대학원 생활을 마무리할 수 있게 큰 도움을 준 이화련, 김성아에게 특별히 깊은 감사를 드립니다. 진심으로 정말 고맙습니다. 덧붙여 많은 시간을 함께했던 동료들에게 감사드립니다. 여러분 같이 대단한 사람들이 모인 이 곳에서 서로의 생각을 나눌 수 있어 영광이었습니다. 김재환, 최준식, Shiva Kumar Arumugasamy, 최재호, 양세준, 전경화, 그리고 한유빈에게 마음을 담은 감사를 드립니다. 마지막으로 힘든 와중에도 내색하지 않고 묵묵히 연구하는 후배들을 응원합니다. 한예지, 유다연, 강지운의 미래에 늘 좋은 일만 있기를 기원합니다. 그리고 그 외에도 저에게 영감을 주었던 수많은 사람들께 감사를 표합니다.

오직 학업에만 집중할 수 있게 모든 면에서 아낌없이 지원해주신 아버지, 어머니께 무한한 감사를 드립니다. 힘들 때 의지할 수 있는 기둥이 되어준 누나, 그리고 매형에게 감사드립니다. 우리 가족에 대한 감사를 모두 글로 적기에는 공간이 모자랄 듯 합니다. 언제나 저의 선택을 믿고 지지하는 우리 가족의 끝없는 응원이 있었기 때문에 제가 오늘까지 버텨낼 수 있었습니다. 우리 가족 모두 정말 고맙고, 존경하고, 그리고 사랑합니다.

2023 년 2 월

신동혁